The Abdus Salam
International Centre for Theoretical Physics

United Nations
Educational, Scientific and
Cultural Organization

IAEA
International Atomic Energy Agency

1968-1

Conference on Teleconnections in the Atmosphere and Oceans

17 - 20 November 2008

The Role of Air-sea interaction in the Climatological Evolution and ENSO-related Variability of the Summer Monsoon over South China Sea and Western Pacific

Ngar-Cheung LAU
NOAA/Geophysical Fluid Dynamics Laboratory
Princeton University
Princeton
New Jersey
USA

A Model Investigation of the Role of Air-Sea Interaction in the Climatological Evolution and ENSO-Related Variability of the Summer Monsoon over South China Sea and Western North Pacific

NGAR-CHEUNG LAU AND MARY-JO NATH

NOAA/Geophysical Fluid Dynamics Laboratory
Princeton University
Princeton, New Jersey

Email: Gabriel.Lau@noaa.gov

Journal of Climate

July 2008

ABSTRACT

The processes contributing to the summertime northeastward march of the climatological maritime monsoon over the South China Sea (SCS) and subtropical western North Pacific (WNP) are examined using the output from a 200-year integration of a coupled atmosphere-ocean general circulation model (GCM). Increased cloud cover and surface wind speed during monsoon onset over SCS in May-June reduce the incoming shortwave flux and enhance the upward latent heat flux at the ocean surface, thereby cooling the local sea surface temperature (SST). The resulting east-west gradient in the SST pattern, with lower temperature in SCS and higher temperature in WNP, is conducive to eastward migration of the monsoon precipitation over this region. Upon arrival of the precipitation center at WNP in July-August, the local circulation changes lead to weakening of the Meiyu-Baiu rainband near 30°N. The subsequent increases in the local shortwave flux and SST impart a northward tendency to the evolution of the WNP monsoon. Many of these model inferences are supported by a parallel analysis of various observational datasets.

The modulation of the above climatological scenario by El Niño-Southern Oscillation (ENSO) events is investigated by diagnosing the output from the coupled GCM, and from experiments based on the atmospheric component of this GCM with SST forcings being prescribed separately in the SCS/WNP and equatorial Pacific domains. During the May-June period after the peak phase of ENSO, the simulated monsoon onset over SCS occurs later (earlier) than normal in El Niño (La Niña) events. These changes are primarily remote responses to the anomalous SST forcing in the equatorial Pacific. The above-normal precipitation in SCS in the ensuing July-August period of the warm events is mainly forced by the local warm SST anomaly, which is linked to ENSO forcing in the tropical Pacific through an 'atmospheric bridge'. In the July-August period of cold events, the equatorial SST anomaly retains its strength and moves still closer to SCS/WNP. This forcing cooperates with the cold SST anomaly in SCS, and brings about dry conditions in SCS/WNP. The ENSO-related changes in SCS/WNP are associated with above-normal (below-normal) Meiyu-Baiu activity during warm (cold) events.

1. Introduction

In recent years, rapid advances have been made in our understanding of the space-time behavior and underlying physical mechanisms of the Asian monsoon system. Such research efforts, as reviewed in the monographs edited by Chang (2004) and Wang (2006), are facilitated by the enhanced availability of observational, modeling and theoretical tools. Studies of the climatological aspects as well as variability of the Asian monsoon indicate that this complex system may be viewed as a mosaic of several regional components. For instance, by analyzing the evolution of the summer rainy season in various Asia-Pacific sites, Wang and LinHo (2002, see their Fig. 9) have identified the following three main constituents: the Indian monsoon over Arabian Sea/Indian Subcontinent/Bay of Bengal, the maritime monsoon over South China Sea (SCS)/Philippine Sea (PS)/subtropical western North Pacific (WNP)[1], and the East Asian monsoon over China/Korea/southern Japan. The phenomena in each of these subregions (such as monsoon onset and subsequent development, fluctuations on intraseasonal and interannual time scales, etc.) exhibit rather unique characteristics. This geographical dependence bears a strong relationship with the local land-sea configuration and orography.

The thermal contrast between the land surface and the surrounding oceans is evidently a key factor in driving the landward march of the summer monsoon rainfall in the India and China/Korea/Japan sectors. Such land-sea contrasts are much less prominent in the mostly maritime zone of SCS and WNP. Nonetheless, the observational findings presented by Wang (1994), Murakami and Matsumoto (1994), Wu and Wang (2001), Wu (2002) and Wang and LinHo (2002) indicate that the monsoon precipitation in that region displays a notable tendency to advance northeastward, with onsets over SCS, PS and WNP typically occurring in mid-May, mid-June and the latter half of July, respectively. Wu (2002) noted that the warmest climatological sea surface temperature (SST) in that region also follows a similar southwest-to-northeast path during the May-July period. The climatological evolution of the precipitation field in the SCS/WNP region is hence modulated by the development of

[1] We shall henceforth use the label WNP to refer to the maritime region within 10°-30°N 120°-160°E.

the underlying SST conditions and the associated thermal gradients, in accord with the hypothesis put forth previously by Murakami and Matsumoto (1994). Wu and Wang (2001) and Wu (2002) further demonstrated that the SST pattern in the SCS/WNP region is in turn influenced by the seasonal march of the local precipitation and atmospheric circulation, which alter the intensity of incoming solar radiation and latent heat flux at the ocean surface. The empirical evidence gathered thus far indicates that two-way air-sea interactions play a substantial role in the spatiotemporal development of the SCS/WNP summer monsoon.

Not only does the atmosphere-ocean coupling in the SCS/WNP sector affect the local monsoon climate, it also has strong implications on the atmospheric environment in the neighboring regions, particularly the East Asian monsoon in the China/Korea/Japan sector. Specifically, the northeastward advance of the SCS/WNP monsoon influences the location and strength of the low-level subtropical anticyclone over the western Pacific (Wu 2002). The latter feature is in turn closely related to the meridional movement and intensity of the Plum Rain (Meiyu-Baiu) phenomenon over China and Japan (e.g., Ding 2004). Hence strong interactions exist between the SCS/WNP and East Asian monsoon systems.

The evolution of the precipitation and SST fields in the SCS/WNP region in individual summers exhibits considerable departures from the climatological scenario as portrayed in the preceding paragraphs. One of the key factors contributing to this interannual variability is the amplitude and phase of the El Niño-Southern Oscillation (ENSO) in the equatorial Pacific. Diagnosis of the observational records by Wu and Wang (2000) indicates that the onset of monsoon rain over SCS and the subsequent northeastward march of this precipitation center to WNP are typically delayed by several pentads in the summers following the peak phase of warm ENSO events; whereas the onsets occur earlier than normal in the summers following cold events. These ENSO-related precipitation anomalies are accompanied by spatial displacement and intensity changes of the subtropical ridge over the WNP, as well as the meridional structure of the monsoon rainbelts over southeastern and central China (Shen and Lau,. 1995;

Chang et al., 2000a, 2000b). The observational evidence presented in these and other studies suggests that the atmospheric and oceanic variations in SCS/WNP serve as a conduit linking ENSO signals in the tropical Pacific to the weather and climate patterns over the populated regions of East Asia.

Wu and Wang (2000) investigated the processes contributing to the relationships between ENSO and the SCS/WNP monsoon by examining the response of an atmospheric general circulation model (GCM) to ENSO-related SST anomalies prescribed in two sites: the equatorial eastern-central Pacific; and the SCS/WNP sector, where the oceanic conditions are linked to remote ENSO forcing by an 'atmospheric bridge' (Klein et al. 1999 and Lau and Nath 2003). The model analysis of Wu and Wang (2000) suggests that the circulation and rainfall patterns in SCS/WNP are affected by the SST variability in both of the above-mentioned regions.

The primary focus of the present study is to further delineate the mechanisms contributing to the climatological seasonal march of the SCS/WNP summer monsoon, and the modulation of this normal evolution by ENSO variability. Our effort is built on the foundation laid by the observational and modeling works reviewed in the preceding paragraphs. The principal tool for this investigation is the current generation of GCMs developed at the Geophysical Fluid Dynamics Laboratory (GFDL). In view of the effects of air-sea interaction on both the climatology and interannual variability of the SCS/WNP monsoon, much of our attention is devoted to the inferences drawn from a 200-year simulation with a fully coupled atmosphere-ocean model. Auxiliary experiments with an atmosphere-only GCM are also conducted and analyzed, with the goal of assessing the relative impacts of remote and in situ SST forcing on the SCS/WNP monsoon. An attempt is also made to compare our model results with available observations and with findings reported in previous studies on this subject.

The GCM tools employed in this study, as well as the observational datasets used for validating the model results, are described in Section 2. The nature of the air-sea coupling associated with the northeastward advance of the simulated and observed SCS/WNP monsoon is analyzed in Sections 3 and 4. Findings on the perturbations of onset dates of the SCS/WNP during ENSO episodes, and on the

concomitant changes in the local atmospheric circulation in various stages of the warm season, are presented in Section 5. Contributions to these variations due to seasonal development of SST forcings from the eastern-central equatorial Pacific and from SCS/WNP are examined in Section 6. The main conclusions of this work are summarized and discussed in Section 7.

2. Model specifications and observational datasets

Most of the model results shown here are based on a 200-year segment from a longer integration of version CM2.1 of a global GCM with full atmosphere-ocean coupling. The formulation of this model and essential aspects of the simulated climate system are documented by Delworth et al. (2006). The fidelity of the tropical Pacific climate and various ENSO phenomena appearing in this simulation is evaluated by Wittenberg et al. (2006). The atmospheric component of this coupled model uses a finite volume dynamical core (AM2.1) written by Lin (2004), with a horizontal resolution of approximately 2° of latitude by 2.5° of longitude, and 24 vertical layers. The physical processes incorporated in the atmospheric and land subsystems of the model are modified versions of those described previously by GFDL Global Atmosphere Model Development Team (2004) and Milly and Shmakin (2002), respectively. The numerics and physical parameterizations used in the oceanic component are based on the fourth generation of the Modular Ocean Model (MOM4) coded by Griffies et al. (2003). This ocean model has a basic horizontal resolution of 1° in latitude and longitude, and 50 vertical layers. In the zonal band between 30°S and 30°N, the meridional resolution increases progressively towards the equator, where the grid spacing reaches 1/3°. Flux exchanges between the atmosphere, ocean, land and sea ice components are computed at 2-hour intervals. Our model analysis is focused on a multi-century control integration of CM2.1 under constant radiative forcing in 1860 (see Table 1 of Delworth et al. 2006).

The model findings are compared with the following observational datasets:

• Horizontal wind at 10-m height and 850 mb from the reanalysis products of the European Centre for Medium-Range Weather Forecasts (ERA40) for the 1960-2000 period (Uppala et al. 2005).

• Precipitation rate compiled by the Global Precipitation Climatology Project (GPCP) for the 1979-2005 period (Huffman et al. 1997, Adler et al. 2003). Pentadal means are based on version 1 of this dataset, and are downloaded from the NOAA National Climatic Data Center website. Monthly means are based on version 2 of this dataset, and are downloaded from the website maintained by the Physical Sciences Division of the NOAA Earth System Research Laboratory.

• Long-term averaged SST for individual calendar days, based on the analyses by Reynolds and Smith (1994) for the 1968-1996 period, and downloaded from the website maintained by the Physical Sciences Division of the NOAA Earth System Research Laboratory.

• Shortwave and longwave radiative fluxes at the ocean surface from the International Satellite Cloud Climatology Project (ISCCP) for the 1984-2004 period (Zhang et al., 2004).

• Latent and sensible heat fluxes at the ocean surface (OAFlux), as analyzed by Yu and Weller (2007) for the 1981-2002 period.

The statistical significance of the anomalies to be presented in Sections 4-6 is estimated by subjecting the signals to a two-tailed Student's *t*-test. Anomalies at or above the 90% or 95% significance level are indicated using various graphical aids, as explained in the captions for Figs. 6-11.

3. Climatological march of the spatial patterns related to the summer monsoon in SCS/WNP

a. Principal circulation and precipitation features

A broad impression of the essential features associated with the summer monsoon in the SCS/WNP sector may be gained from the climatological charts in Fig. 1, which shows the simulated and observed distributions of horizontal wind vector at 10-m height and precipitation for the periods of May-June and July-August. In May-June, a cyclonic low-level circulation prevails over the SCS in the model atmosphere (Fig. 1a). This flow pattern is accompanied by enhanced precipitation in the eastern portion of the SCS. In contrast, much of the PS and subtropical WNP are under the influence of an expansive anticyclone, with a prominent dry zone in 15°-30°N and 130°-160°E. Situated to the northwest of this surface anticyclone is an elongated belt of heavy precipitation, which extends northeastward from China

to southern Japan. The northward or northeastward flows on the southern flank of this rainband serve to transport moisture from the nearby SCS and East China Sea. Most of the above simulated monsoon features are in agreement with those appearing in the observed pattern (Fig. 1c). The observed subtropical rainbelt in the China/Japan sector, often referred by local meteorologists as the 'Meiyu-Baiu' (or Plum Rain) phenomenon (e.g., Ding and Chan 2005), is characterized by higher precipitation rates and a stronger spatial coherence than its model counterpart.

In July-August, the simulated cyclonic flow pattern associated with the monsoon trough over SCS spreads eastward, and covers a large portion of the PS and East China Sea (Fig. 1b). The subtropical ridge over WNP accordingly retreats eastward. The axis of this ridge migrates northward by 5°-10° of latitude. These circulation changes are accompanied by precipitation increases over the Philippines and the WNP within the 10°-20°N belt, northward displacement and reduction in areal extent of the dry zone associated with the subtropical anticyclone over the WNP, as well as decrease (increase) in precipitation over central (northeastern) China. The GPCP dataset (Fig. 1d) indicates higher rainfall rates over WNP near 10°N 135°W, East China Sea and the Korean Peninsula than the model simulation. The northward advance of the elongated Meiyu-Baiu rainbelt from early to later summer is more evident in the observed patterns than in the model charts.

b. Detailed evolution of monsoon features and relationships with surface fluxes

In order to highlight the more rapid variations occurring in the course of the seasonal march, consecutive 10-day averages of selected fields are computed, and the changes from one 10-day period to the next are examined. In the left panels of Fig. 2 are shown the distributions of these tendencies in precipitation and 850-mb vector wind, as obtained by subtracting the climatological CM2.1 data for the 10-day period near the end of each calendar month in the warm season from the corresponding data for the succeeding 10-day period. Inspection of these panels reveals the systematic northeastward movement of a positive precipitation tendency center in the model atmosphere from Indochina in early May (Fig. 2a), to SCS in early June (Fig. 2b), to PS in early July (Fig. 2c), and to WNP in early August

(Fig. 2d). Cyclonic tendencies of the 850-mb wind prevail to the northwest of the sites of strongest precipitation changes, in accord with the circulation response to tropical heat sources in idealized mechanistic models (e.g., Gill 1980). These cyclonic tendencies are accompanied by easterly or northeasterly wind changes near 30°N 120°-150°E in Fig. 2c, and over central China and Yellow Sea in Fig. 2d. The circulation changes in these regions impede the prevalent northeastward transport of moisture from SCS and East China Sea in early summer (see Fig. 1a), and are hence coincident with negative precipitation tendencies (see shading in Figs. 2c,d).

The implications of the circulation and precipitation changes on the fluxes at the ocean surface are studied by plotting the tendencies of simulated downward shortwave (SW) radiative flux (middle column of Fig. 2) and upward latent heat (LH) flux (right column), for the same set of 10-day averages used in constructing the left column. The sign convention adopted here is such that positive tendencies in SW (LH) flux would lead to oceanic warming (cooling). Analogous computations based on model data for longwave radiative flux and sensible heat flux (not shown) yield much weaker tendencies as compared to those associated with the SW and LH fluxes.

A strong spatial correspondence exists between the shaded patterns in the left and middle columns of Fig. 2, with positive precipitation tendency being associated with reduced downward SW flux, and vice versa. This relationship is attributable to the impact of precipitation changes on the local cloud cover, which in turn modulates the intensity of solar radiation arriving at the ocean surface. Within the tropical and subtropical zones, the distribution of the LH flux tendency (right column of Fig. 2) is linked to changes in the local surface wind speed and sea-to-air humidity gradients through the parameterization scheme for surface fluxes (Beljaars 1995). Increased wind speeds, as would occur when the wind tendency vector (left column of Fig. 2) has a similar orientation as the local climatological wind vector (left column of Fig. 1), lead to enhanced upward transfer of LH. Conversely, opposition of the wind tendency to the mean flow results in reduction of wind speed and LH flux.

During the May-June period, the arrival of monsoon rainfall at SCS (Figs. 2a,b) is accompanied by enhanced cloud cover and decreased SW flux (Figs. 2e,f). As a consequence of the strengthening of the southwesterly flow over this region (Figs. 2a,b), the heat loss from the SCS to the atmosphere through LH transfer increases (Figs. 2i,j). These tendencies in both SW and LH fluxes are conducive to cooling of the ocean surface in SCS. In contrast, the relatively weak precipitation tendencies over the 20°-30°N belt in WNP during May-June are coincident with positive tendencies in SW flux and surface warming. In early May, the reduced LH flux over much of the subtropical WNP (Fig. 2i) also contributes to warming tendencies of the local waters.

As the center of the positive precipitation tendency continues to migrate towards PS and WNP in July-August (Figs. 2c,d), the amount of SW radiation arriving at the latter maritime regions is reduced (note negative tendencies in Figs. 2g,h). As noted earlier, a zonally oriented belt of easterly wind tendency and reduced precipitation is seen to develop farther north of the wet zone, thus leading to increased SW flux within 25°-40°N. The SST cooling resulting from the reduced SW flux in the 10°-20°N belt is partially offset by the oceanic warming due to reduced LH loss at the same sites (Figs. 2k,l). Analogously, the warming effects of the increased SW flux in the 25°-40°N zone in Figs. 2g,h are opposed by cooling tendencies due to LH flux changes in the same regions

In summary, the model results in Fig. 2 are consistent with the observational findings presented by Wu (2002) on the role of air-sea coupling in the climatological evolution of the summer monsoon within the SCS/PS/WNP domain, as portrayed in the schematic diagram and flow chart in his Figs. 11 and 12, respectively. The increasing intensity of precipitation and monsoon flow over SCS during May-June leads to local SST cooling through modulation of SW and LH fluxes; whereas oceanic warming proceeds in several parts of PS, East China Sea and WNP during the same period. Under the influence of the resultant east-west gradient of SST changes, the precipitation center migrates eastward towards the relatively warmer waters. A north-south oriented dipole pattern in the vector wind tendency and precipitation fields is then established in the East Asia/WNP sector. The changes in SW and LH fluxes

associated with this development yield meridional contrasts in SST tendencies, with oceanic cooling near the precipitating zone, and warming farther north. This configuration of SST changes imparts a northward component to the movement of the precipitation center over WNP.

The model results in Fig. 2 may be evaluated using observational patterns based on the datasets listed in Section 2. The tendency from June 20-29 to June 30-July 9 is shown in Fig. 3 for observed (a) precipitation and 850-mb wind vector, (b) SW flux and (c) LH flux. Both observations (Fig. 3) and model (Figs. 2c,g,k) indicate drying tendencies over the central portion of SCS, as well as increasing rainfall and cyclonic circulation to the northeast of the Philippines. The dry band and anticyclonic flow developing near 30°N are evident in Figs. 2c and 3a. In the PS/WNP domain, the observed patterns for SW and LH fluxes exhibit negative tendencies near 10°-20°N, and positive tendencies near 25°-35°N (Figs. 3b,c), in support of the dipolar distribution based on the model results (Figs. 2g,k).

4. Temporal development of climatological SCS/WNP monsoon in zonal and meridional directions

To delineate the detailed evolution of the SCS/WNP monsoon, latitudinal averages of various climatological fields are computed at 5-day (pentad) intervals. At a given longitude between 100°E and 160°E, these averages are taken over a band with a latitudinal width of 10°. The northern and southern limits of this band (shown as red segments in Figs. 2a-d) are shifted progressively poleward with increasing longitude, so as to accommodate the southwest-to-northeast orientation of the migration path of the wet zone. The pentadal and latitudinal averages are then plotted as a function of time and longitude. Model and observed patterns are shown in Fig. 4 for (a, e) precipitation and 850-mb wind vector, (b, f) SW flux, (c, g) LH flux, and (d, h) SST.

In the model atmosphere, the earliest precipitation signal in the domain under consideration appears near 100°-110°E (i.e., southern Indochina) in mid-May (Fig. 4a). The rainfall increases markedly within 115°-125°E (eastern SCS and the Philippines) in June; whereas the WNP east of 130°E remains dry during this period. The precipitation rate in the latter region intensifies in July-August. The

northeastward spread of the precipitation maximum is accompanied by advances of the 850-mb southwesterlies from SCS to WNP, and the attendant retreat of the easterlies over WNP.

The arrival of the SCS monsoon in May-June is coincident with increased cloud cover and reduced incoming solar radiation within the 110°-120°E zone. The SW flux over SCS decreases by 40-50 Wm^{-2} in this period (Fig. 4b). The attenuation of the SW flux over PS and WNP occurs noticeably later than the corresponding changes over SCS. The timing of this development is evidently related to the northeastward march of the precipitation signal over this domain (see Fig. 4a).

The strengthening of the SCS monsoon in May-June results in higher surface wind speeds and an increase in LH flux of about 20-30 Wm^{-2} within 110°-120°E during that period (Fig. 4c). The magnitude of the changes in LH flux in PS and WNP is comparatively weaker.

In accord with the decreasing SW flux and increasing LH flux over the SCS sector during the May-June period, the SST within 110°-120°E rises to a peak in early June, and drops gradually in July (Fig. 4d). In contrast, the SST in PS and WNP continues to increase through the June-July period, and attains peak values in mid-August. The results in Fig. 4d portrays a sharp contrast between the SST pattern in June, when the surface waters in SCS is relatively warmer than those in PS/WNP, and the corresponding pattern in July-August, when the east-west gradient is reversed.

The essential aspects of the time-space evolution of various model signals in the left column are also discernible in the observed patterns presented in right column. Particularly noteworthy are the northeastward advance of the observed precipitation and southwesterly flow across the SCS/WNP domain during the June-August period (Fig. 4e); the diminishing SW flux over SCS during May-June, and in 125°-135°E about one month later (Fig. 4f); enhancement of the LH flux over SCS during May-June (Fig. 4g); and reversal of the east-west SST gradient across SCS and PS/WNP in the course of the summer season (Fig. 4h). The SST maximum and initiation of the wet period in eastern SCS occurs earlier in the observed atmosphere than in the model simulation. The peak observed precipitation rate and SST in WNP also take place several pentads earlier than the corresponding model features. The dry

zone near 110°E (off the Vietnamese coast), which is partially related to local coastal upwelling (see cold SST at that longitude in Fig. 4h), is more prominent in the observed pattern than in the model atmosphere.

The detailed development in the meridional direction of the monsoon features over WNP is examined in Fig. 5, which shows pentadal data for simulated and observed (a, c) precipitation and 850-mb wind vector and (b, d) 10-day tendency of SW flux, as a function of time and latitude. For a given latitude, averages of these data are taken over the longitudinal zone from 120°E to 150°E.

In the model atmosphere (Fig. 5a), the axis of the primary rainbelt in the WNP sector migrates northward from about 5°N in early June to about 15°N in August. The prevalent 850-mb circulation within this rainbelt is seen to switch from an easterly pattern in early summer to a southwesterly pattern in August. In the July-August period, the cyclonic development of the flow pattern in the 10°-25°N zone may be inferred from the counterclockwise turning of the wind vectors when they are scanned from south to north across this zone. Located immediately to the north of the main WNP precipitation belt is a dry region with anticyclonic meridional wind shear (note clockwise turning of the vectors with increasing latitude). The characteristics of this dry zone are closely related to the subtropical ridge over WNP (see Fig. 1). The patterns in Fig. 5a offer additional evidence on the poleward migration of the axis of this anticyclone from about 20°N in June to 35°N in August. During the June-July period, a secondary rainband with prevalent southwesterly flow is discernible to the north of the subtropical high. This precipitation feature is centered near 30°N in June, and corresponds to the eastern extension of the Meiyu-Baiu front.

Comparison between the shading patterns in Figs. 5a,b indicates that positive SW flux tendencies are collocated with sites of decreasing precipitation associated with the development of the subtropical anticyclone. Conversely, the enhanced rainfall at the primary WNP rainbelt and Meiyu-Baiu front leads to negative tendencies in SW flux.

The model results in the left column Fig. 5 may be checked against the corresponding observations in the right column. The timing and location of the principal precipitation features, as well as the accompanying wind circulation and changes in SW flux, are similar in simulated and observed patterns. The observed rainfall rates near the Meiyu-Baiu front are higher than those simulated by CM2.1; whereas precipitation intensity of the primary WNP rainbelt in 5°-20°N in the model is too strong when compared with the observations.

5. Impact of ENSO on the evolution of the SCS/WNP monsoon

Outstanding ENSO events appearing in the CM2.1 simulation are selected using a procedure similar to that adopted in Lau et al. (2008)[2]. The general characteristics of ENSO events appearing in the CM2.1 integration are analyzed by Wittenberg et al. (2006). The evolution of ENSO-related atmospheric and oceanic anomalies in this model is similar to the observed development in many respects. However, the amplitude of the simulated equatorial SST perturbations is too strong, and the principal ENSO signals are displaced too far west of the observed locations. Joseph and Nigam (2006), Guilyardi (2006), among others, have also compared the performance of CM2.1 in reproducing various ENSO features with that of various models developed at other centers.

a. *Evolution of rainfall over SCS and PS in El Niño and La Niña events*

Areal averages of the precipitation rates in various pentads of the calendar year are computed for two individual rectangular sites. The first region (8°-18°N 115°-120°E; hereafter referred as Site A)

[2] An index of the SST fluctuations in the central equatorial Pacific is constructed by averaging the monthly SST anomalies over the domain within 5°S-5°N 120°-170°W. The time series of this index is smoothed by computing 5-month running means. A warm (cold) ENSO event is identified when the SST index exceed the thresholds of 0.4°C (-0.4°C) for 6 consecutive months or longer. In a majority of the events that satisfy this criterion, the SST index first reaches the threshold value near the beginning of a given year [hereafter referred as the year of initiation or Year(0)]. This index then attains maximum amplitude towards the end of Year(0), or the beginning of the following year [hereafter referred as Year(1)], and finally falls below the threshold value in the middle of Year(1). Only those events that follow this general evolutionary pattern are chosen. In some instances, the smoothed SST index exceeds the ±0.4C threshold for more than 16 months. For such cases, if the extremum of this index occurs in the August-December period of a certain year, that year is designated as Year(0), and the following year is labeled as Year(1); if the extremum occurs in the January-May period of a year, that year is designated as Year(1), and the preceding year is referred as Year(0). Prolonged events with the index peaking in June-July are discarded due to ambiguities in assigning the labels of Year(0) and Year(1) to these events. This procedure yields altogether 34 warm events and 45 cold events. We shall henceforth refer to the temporal phase of the ENSO events by using a label that consists of the first three letters of the month for that phase, followed by the year indicator (0 or 1) in parentheses. For instance, May(1) refers to the month of May in Year(1).

lies in eastern SCS. The second region (10°-20°N 125°-130°E; labeled as Site B) is located immediately to the east of the Philippines. The boundaries of these sites are depicted in Fig. 2a. In Fig. 6 is shown the pentadal variations of the precipitation at (a) Site A and (b) Site B. Results based on 200-year climatological averages are displayed using black solid curves; whereas the time series based on composites over the data for Year(1) of selected 34 warm and 45 cold ENSO events are represented by the red (blue) dashed curves, respectively. We shall hereafter refer to the composites over El Niño and La Niña events as warm and cold composites, respectively.

Comparison of the time series in Fig. 6a with those in Fig. 6b reveals that, for a given data group (i.e., climatology, warm composite, or cold composite), the peak in rainfall rate at Site A occurs at about 3 pentads before the precipitation at Site B reaches its maximum level. The temporal lag between the climatological precipitation signals at SCS and PS (solid black curves in Fig. 6) is consistent with the northeastward development of the monsoon rains across this region. The evidence of an analogous lag between the pair of dashed red curves (warm composite) for Sites A and B, as well as between the dashed blue curves (cold composite), implies that the *spatial* evolution of the SCS/WNP monsoon in ENSO years also follows a similar southwest-to-northeast path as the long-term averaged scenario. However, the results in Fig. 6 illustrate that the specific *timing* of this evolution during warm or cold events is markedly different from climatology. In particular, for a given site (A or B), the occurrence of the precipitation peak during warm ENSO events is typically delayed relative to the corresponding climatological peak by several pentads. Conversely, maximum precipitation in cold events precedes the climatological peak by several pentads. These model results are in agreement with the observational analyses performed by Wu and Wang (2000), who similarly noted a temporal lag (lead) of 2-5 pentads of the monsoon rainfall evolution in SCS/WNP during warm (cold) events versus the climatological development.

b. Asymmetry in El Niño and La Niña development

A key factor in determining the anomalous precipitation pattern in SCS/WNP during ENSO events is the evolution of the SST forcing in the equatorial Pacific. The dependence of the monthly SST anomalies averaged over the 5°S-5°N zone on longitude and temporal phase of the ENSO cycle is portrayed in Fig. 7, for composites of (a) warm and (b) cold events in the CM2.1 simulation.

The distribution in Fig. 7a illustrates that the largest positive SST anomalies in boreal spring and early summer of Year(1) are simulated to the east of 150°W during the warm events, and that the SST anomalies near and to the west of the dateline are relatively weaker in the same period. This tendency for the warm SST anomaly center to migrate eastward with time during the first half of Year(1) is in sharp contrast to the corresponding development in simulated cold events (Fig. 7b). The latter composite indicates westward advancement of the cold anomaly in May(1)-Aug(1), with stronger SST amplitudes near and to the west of the dateline, and weaker signals east of 120°W.

The above findings on the asymmetries in SST evolution in simulated warm and cold events may be compared with the observational results presented by Larkin and Harrison (2002, see their Fig. 8). In support of the model results, the observations also indicate that the anomalous SST extremum in Year(1) of warm events is located east of the corresponding feature in cold events; and that the transition from warm to cold phase takes place earlier in Year(1) than the transition from cold to warm phase. These asymmetries lead to a relatively more distinct and persistent cold SST anomaly in the western equatorial Pacific during the boreal summer of Year(1) in observed La Niña events, as compared to the warm anomaly in observed El Niño episodes.

Some understanding of the eastward (westward) advance of SST anomalies in simulated warm (cold) events (Fig. 7) may be gained by considering the pertinent terms in the equation for the SST budget, which determines the propagation characteristics of the 'SST modes' of ENSO development (e.g., see reviews by Neelin et al. 1998, Wittenberg 2002 and Wang and Picaut 2004). In particular, we focus on the contributions of the nonlinear advection terms, $-u'T_x'$ and $-w'T_z'$ (A.T. Wittenberg, personal communication). Here u, w are the surface ocean current speeds in the zonal (x) and vertical (z)

directions, respectively; T_x, T_z the partial derivatives of the ocean surface temperature T with respect to x and z, respectively; and the prime represents the anomalous component. During an El Niño event, the anomalous eastward wind stress to the west of the warm SST center leads to anomalous eastward surface current ($u' > 0$) and downwelling ($w' < 0$) (e.g., see Fig. 11 of Neelin et al. 1998). The eastward and downward penetration of warm surface waters during warm events also alter the zonal and vertical temperature gradients, so that $T_x' > 0$ and $T_z' < 0$. Hence $-u'T_x' < 0$ and $-w'T_z' < 0$ to the west of the warm SST anomaly. The cooling at that location is conducive to an eastward tendency of the warm anomaly. An and Jin (2004) have similarly noted the roles of the $-u'T_x'$ and $-w'T_z'$ terms in the eastward migration of the SST anomaly in the outstanding 1982/83 and 1997/98 El Niño events. Conversely, the anomalous westward wind stress to the west of the cold SST center during La Niña is associated with $u' < 0$ and $w' > 0$. The modified distribution of the oceanic temperature gradient is characterized by $T_x' < 0$ and $T_z' > 0$. The terms $-u'T_x'$, $-w'T_z'$ are again negative to the west of the cold anomaly, and therefore lead to westward migration of this SST signal. The contributions of these nonlinear effects to the SST budget are particularly significant during strong ENSO events, when large perturbations to the temperature gradients (i.e., T_x' and T_z') occur. The prominence of eastward (westward) SST propagation during the simulated warm (cold) events (Fig. 7) partially results from the excessive amplitude of the SST variability related to ENSO phenomena in CM2.1 (Wittenberg et al. 2006).

c. Anomalous circulation and precipitation patterns in warm and cold events

The implications of the distinctive SST development in the warm and cold phases of ENSO on the anomalous atmospheric circulation and precipitation patterns in SCS/WNP are explored in Fig. 8 using composite charts for the El Niño (left panels) and La Niña (right panels) events as identified in the CM2.1 simulation. Model anomalies are shown for the months of May(1) (top two rows) and Jul(1) (bottom two rows). Results are presented for SST (shading), and 200-mb velocity potential χ and divergent circulation $\mathbf{V}_\chi$ (contours and arrows, respectively) in Figs. 8a,c,e,g, and for precipitation (shading) and 850-mb streamlines in Figs. 8b,d,f,h.

In the May(1) composite of the warm events, the SST pattern in the tropical western Pacific (shading in Fig. 8a) consists of an elongated near-equatorial positive anomaly extending east of about 160°E, and a pair of negative anomalies centered near 15°N 165°E and 10°S 180°E. This configuration is similar to observations for this phase of ENSO development (e.g., see Harrison and Larkin 1998 and Alexander et al. 2004), except that the simulated warm anomaly is displaced to the west of its observed location. The SST in much of SCS and the eastern Indian Ocean is above normal, partially due to the enhanced SW flux associated with the anomalous sinking branch of the prevalent Walker-type circulation during El Niño events. The corresponding distributions of χ and $\mathbf{V}_\chi$ at 200 mb (contours and arrows in Fig. 8a) indicate anomalous large-scale divergence from the site of the equatorial warm SST zone. This region is collocated with enhanced precipitation, and anomalous westerlies at 850 mb (Fig. 8b). Large-scale convergence at 200 mb occurs along a broad subtropical belt stretching from SCS to 150°W, where dry conditions and low-level anticyclonic flows prevail. Situated still farther north of this anomalous ridge is a cyclonic cell, with axis located in the 35°-45°N band. This extratropical feature and the subtropical ridge to its south straddle an anomalous westerly or southwesterly zone at 25°-35°N, with above-normal precipitation. The pair of circulation cells at 850 mb in subtropical and extratropical North Pacific with opposing vorticity changes is reminiscent of the 'Pacific-Japan' teleconnection pattern associated with variations of convective activities over WNP (Nitta 1987).

Due to the continuous eastward displacement of the SST signal in the boreal summer of Year(1) in the simulated warm events, and the rapid phase transition from El Niño to La Niña within this period (see Fig. 7a), the positive SST anomaly in the equatorial Pacific is much diminished in Jul(1) (Fig. 8c). On the contrary, the warm conditions in SCS persist through the May(1)-Jul(1) period. The altered SST anomaly pattern in Fig. 8c is accompanied by substantially weakened upper level divergence from the equatorial central Pacific, northeastward shift of the 200-mb convergence center (as inferred from the maximum in χ) over WNP, and the prevalence of divergent flows over SCS. These circulation changes in the upper troposphere are in turn associated with weak precipitation anomalies within the equatorial

zone, northward shift of the axes of the dry 850-mb subtropical ridge over WNP, and a corresponding poleward migration of the elongated wet zone lying on the northern flank of this ridge. Over the SCS, the low-level circulation is no longer under the influence of an anticyclonic regime, and the precipitation anomaly switches from below-normal in May(1) to above-normal in Jul(1) (see red curve in Fig. 6a).

The negative SST anomaly in the equatorial Pacific in May(1) of the composite cold events (Fig. 8e) has a higher amplitude and extends farther to the west than the corresponding positive anomaly in the warm composite (Fig. 8a). Most of the other features in the warm composite for May(1) (Figs. 8a,b) are also discernible in the cold composite (Figs. 8e,f), but with reversed polarity.

In sharp contrast to El Niño development (Figs. 7a and 8c), the negative SST anomaly in cold events retains much of its strength through the boreal summer of Year(1), and continues to migrate westward in this period (Figs. 7b and 8g). Consequently, the SST pattern in Jul(1) is dominated by negative anomalies throughout the western equatorial Pacific and SCS. The amplitudes of the circulation and precipitation anomalies over these regions (Figs. 8g,h) are notably higher than those in the warm composites (Figs. 8c,d). This development leads to significant negative departures of the precipitation in cold events at Sites A and B from climatology in Jul(1)-Aug(1) (Figs. 6a,b). The low-level circulation pattern in Fig. 8h is characterized by anomalous anticyclonic flows over SCS and a cyclonic center near 30°N 135°E. The dry anomaly situated over southeastern China in May(1) (Fig. 8f) is seen to migrate towards the Korea/southern Japan sector two months later (Fig. 8h).

The westward displacement of the simulated dry anomaly over the equatorial western Pacific in cold events (Fig. 8f) relative to the wet anomaly in warm events (Fig. 8b) is consistent with the observational findings of Hoerling et al. (1997) on the asymmetries between the two opposing phases of ENSO. The simulation of strengthened (weakened) subtropical anticyclone over WNP and Meiyu-Baiu activity in Year(1) of El Niño (La Niña) events, as illustrated in Fig. 8, is supported by the observational evidence presented by Shen and Lau (1995) and Chang et al. (2000a, 2000b).

6. Contrasting the effects of remote and local SST forcing on the SCS/WNP monsoon

a. Experimental Design

The overall model evidence presented in Fig. 8 suggests that the circulation and rainfall anomalies in the SCS/WNP sector are linked in varying degrees to remote forcing associated with ENSO-related SST changes in the equatorial Pacific, and to local air-sea interactions within SCS/WNP itself. These mechanisms are further explored by direct experimentation with the atmospheric component of CM2.1. This set of integrations entails the prescription of time-varying SST anomalies at the lower boundary of this atmospheric model (AM2.1). The monthly SST data used in this procedure are obtained from the composites of warm and cold events identified in the 200-year simulation with the fully coupled CM2.1 (see details in footnote 2). In each integration, the prescription of SST composite data is performed for the 21-month duration from Mar(0) to Nov(1). Integrations are conducted separately for the composite warm and cold events, and for each of the following prescription domains[3]:

- The tropical Pacific extending from 15°S to 15°N, and from 135°E to the American coasts. The western portion of this domain is depicted using red borders in Figs. 9d and 10d. This integration is hereafter referred as the ENSO experiment.
- The SCS/WNP sector, extending from the East Asian coast to 135°E within the 5°S-15°N band, and to 180°E within the 15°-30°N band. This domain is depicted using red borders in Figs. 9e and 10e. This integration is hereafter referred as the SCS/WNP experiment.
- Combination of the two domains used in the ENSO and SCS/WNP experiments. The western portion of this domain is depicted using red borders in Figs. 9f and 10f. This integration is hereafter referred as the ENSO+SCS/WNP experiment.

In addition to the above experiments, a 30-year integration with AM2.1 has been completed with the climatological seasonal cycle of the SST field being inserted at grid points throughout the World Oceans.

[3] For each of the experiments in this list, the oceanic grid points lying outside of the respective SST prescription domain are constrained to follow the climatological seasonal cycle, as given by the 200-year average of the CM2.1 simulation. To ensure a smooth transition from the region where SST composite data are applied to the region subjected to climatological conditions, the composite data are linearly interpolated to the climatological values over a taper zone with a latitudinal or longitudinal width of about 4°.

This simulation is hereafter referred as the CLIMO experiment. For each of the three prescription domains considered here, the 21-month integrations are repeated 30 times, with initial states being furnished by output from the CLIMO experiment for individual years. The suite of experiments with time-varying SST forcing requires integration over a total of 3 (prescription domains) × 2 (warm and cold composites) × 30 (ensemble members) × 21 (duration) = 3780 months. In the following presentations, the anomalous response of AM2.1 to composite SST forcing prescribed in a specific domain (i.e., ENSO, SCS/WNP or ENSO+SCS/WNP) is obtained by subtracting the 30-year average of the CLIMO simulation from the 30-member ensemble means of the respective experiment.

It should be emphasized that this experimental design is suited for attributing various atmospheric signals to a given SST forcing, but provides no information on the origin of the SST forcing, and does not take into consideration the feedback effects of the atmospheric response on various ocean fields. Douville (2005), Copsey et al. (2006) and other investigators have pointed out the limitations of sensitivity experiments with prescribed SST forcing in reproducing the two-way interactions occurring within the atmosphere-ocean system. The inferences drawn from the suite of AM2.1 integrations described in this section are also dependent on the fidelity of the ENSO-related SST variations as produced by CM2.1. As mentioned in Section 5, this model exhibits biases in the amplitude and spatial pattern of such SST anomalies.

b. Response patterns to SST forcings in equatorial Pacific and SCS/WNP

The departures of χ (contours) and $\mathbf{V}_\chi$ (arrows) at 200 mb and precipitation (shading), as generated in the ENSO, SCS/WNP and ENSO+SCS/WNP experiments, from the corresponding fields simulated in the CLIMO run, are displayed in Fig. 9 for May(1), and in Fig. 10 for Jul(1). Responses to the warm (cold) composite SST forcing are shown in the left (right) panels.

In May(1), the atmospheric response to the SST forcing in the equatorial Pacific, as illustrated in the ENSO experiment (Figs. 9a,d), is notably stronger than the response to the SST changes in the SCS/WNP sector (Figs. 9b,e). Over the SCS/WNP region, and for a given ENSO polarity (El Niño or La

Niña), the divergent circulation responses to local SST forcing and to remote ENSO influences tend to oppose each other. The response in the ENSO+SCS/WNP experiment (Figs. 9c,f) is more similar to that in the ENSO experiment than in the SCS/WNP experiment.

The sum of the responses (not shown) to SST forcings in ENSO and SCS/WNP, as obtained by adding the data in Figs. 9a,b for warm events, and in Figs. 9d,e for cold events, bear a strong resemblance to the response patterns to the combined ENSO and SCS/WNP forcings, shown in Figs. 9c,f. This finding implies that the net response to the SST anomalies imposed in both the ENSO and SCS/WNP regions may be viewed as the linear superposition of the individual responses to these two separate sites. The patterns in Figs. 9c,f also exhibit a considerable correspondence with warm and cold composites based on output from the fully coupled simulation (Figs. 8a,b,e,f). This favorable comparison between the CM2.1 and AM2.1 results lends support to the AM2.1 model as a useful tool for diagnosing the relative roles of different SST forcings in generating atmospheric anomalies related to ENSO.

The spatial correspondence between the response patterns in various AM2.1 and CM2.1 experiments, as described in the preceding paragraph, is quantified by computation of spatial correlation coefficients (SCC) between the anomalous precipitation field in the ENSO+SCS/WNP experiment, and the corresponding field in the ENSO, SCS/WNP, linear sum of ENSO and SCS/WNP, and CM2.1 experiments. The results for warm and cold events in May(1) are displayed in the left half of Table 1. These statistics confirm the strong resemblance among the precipitation features in the ENSO+SCS/WNP, ENSO, sum of ENSO and SCS/WNP, and CM2.1 experiments.

In Jul(1) of warm events (Fig. 10a), the remote influence of the equatorial Pacific SST forcing on the atmospheric conditions near SCS and western Pacific is much reduced. On the other hand, the sustained SST warming in the SCS/WNP sector leads to upper-level divergence and above-normal precipitation in that region (Fig. 10b). The forcing in the SCS/WNP domain apparently makes a much stronger contribution to the total response in the ENSO+SCS/WNP experiment (Fig. 10c) than in

May(1) (see Figs. 9b,c). The model findings support the notion that the delay in the onset of the SCS/WNP monsoon during warm events (Fig. 6) is the consequence of the following chain of events: subsidence and below-normal precipitation over Sites A and B induced remotely by positive SST forcing in the tropical central Pacific in May(1), continued warmth of the surface waters in SCS and WNP due to increased SW flux through the May(1)-Jul(1) period, and enhanced precipitation responding locally to this positive SST anomaly in Jul(1).

The response patterns of the ENSO and SCS/WNP experiments for Jul(1) of the La Niña events (Figs. 10d,e) tend to reinforce each other in the SCS/WNP region, with anomalous 200-mb convergence and dryness being induced by both the persistent cold SST anomaly in the western equatorial Pacific, and the local cold conditions due to the effects of the atmospheric bridge (see Klein et al. 1999). This cooperation between the forcings in ENSO and SCS/WNP leads to an enhanced convergence and dry response in the ENSO+SCS/WNP experiment (Fig. 10f).

The SCC between the precipitation response pattern for Jul(1) in the ENSO+SCS/WNP experiment and that in various other experiments are listed in the right half of Table 1. These results further illustrate the much larger contribution of the SCS/WNP forcing to the total response in Jul(1) as compared to May(1) (see second row of data entries in Table 1). The strong correspondence between the pattern in ENSO+SCS/WNP with the linear sum of the individual responses in ENSO and SCS/WNP (third row), and between the AM2.1 and CM2.1 results (fourth row), as noted previously for May(1), is equally evident in the Jul(1) data.

c. Meridional evolution of precipitation anomalies

The latitudinal development of the major precipitation anomalies in the SCS/WNP sector is examined in greater detail in Fig. 11. The patterns in this figure are based on the methodology used for Fig. 5a, and are shown for (a) warm and (c) cold composite of the CM2.1 data, and for response of AM2.1 to (b) warm and (d) cold composite SST forcing prescribed in the ENSO+SCS/WNP domain. The pattern in Fig. 11a is dominated by the poleward migration of two coherent features: a dry anomaly

with displacement from about 10°N in May(1) to 20°N in Jul(1), and a wet anomaly advancing from 25°N in May(1) to 35°N in Jul(1). As evident from the maps in Figs. 8b,d, the spatial shift of the dry anomaly is closely related to the movement of the anomalous anticyclone in subtropical WNP; whereas the evolution of the wet anomaly follows that of the westerly belt situated immediately to the north of this anticyclone. Inspection of the anomaly pattern in Fig. 11a and its climatological counterpart in Fig. 5a illustrates that the precipitation anomalies in warm events tend to reinforce the poleward movement of the climatological dry zone in subtropical WNP, and the parallel displacement of the Meiyu-Baiu rainbelt farther north.

The above phenomena are simulated with reversed polarity in cold events (Fig. 11c). The behavior of the main rainfall anomalies in the CM2.1 simulation during warm and cold events is replicated in the ENSO+SCS/WNP experiment (Figs. 11b,d). The stronger spatial coherence of the principal features in the CM2.1 results (upper panels of Fig. 11) as compared to those simulated in AM2.1 (lower panels) is suggestive of the role of two-way air-sea coupling in promoting the northward evolution of these precipitation anomalies.

7. Summary and Discussions

The mechanisms contributing to the climatological northeastward advance of the summer maritime monsoon across the SCS/WNP sector are diagnosed on the basis of an extended simulation with a coupled atmosphere-ocean GCM. In the May-June period, the arrival of the monsoon rain over SCS brings about increased cloud cover and surface wind speed over that region. These changes lead to reduced downward SW flux and enhanced upward LH flux at the ocean surface (Figs. 2f,j). Both of these effects result in local SST cooling. At the same time, the waters in PS and WNP continue to warm, mainly due to the prevalent dry and clear-sky conditions, and hence stronger SW fluxes (relative to those over SCS) in that sector. As a consequence of this east-west contrast in surface heating, the prevalent thermal gradient in early summer (with the SST in SCS being warmer than that in WNP) is reversed by July (with WNP warmer than SCS) (Fig. 4d). The precipitation center follows the

movement of the site of maximum SST, so that the rainfall rates over WNP increase markedly in July and August. The positive precipitation changes over WNP are concomitant with easterly or northeasterly tendencies near 30°N, which oppose the prevalent southwesterly airstream that supplies moisture to the Meiyu-Baiu rainband. The reduced Meiyu-Baiu activity near 30°N in July leads to increased SW flux and oceanic warming at that site. The resultant pattern of SST tendency in WNP is conducive to northward movement of the monsoon rainfall in this region (Fig. 5a).

The relationships between ENSO and the development of the summer monsoon over SCS/WNP are explored by partitioning the output from CM2.1 according to El Niño and La Niña events. This composite analysis is augmented by integrations with AM2.1 subjected to SST forcing at different strategic sites. The asymmetric nature of the warm and cold phases of ENSO has strong impacts on the strength and location of the SST forcing in the equatorial Pacific (Fig. 7). The cumulative model evidence indicates that both this remote forcing and the local SST within the SCS/WNP domain play substantial roles in the variability of the SCS/WNP during the summer after the mature stage of ENSO. In warm events, the precipitation over SCS and WNP is suppressed in May-June mainly due to large-scale subsidence forced remotely by SST anomalies residing in the central equatorial Pacific (Fig. 9a). This equatorial forcing weakens considerably in the course of the summer season, so that its influence on the SCS/WNP monsoon is much diminished by July. Meanwhile, the warm anomaly within SCS persists through the May-July period. This local SST forcing plays an ascending role in the latter half of summer, leading to enhanced precipitation over SCS in July-August (Fig. 10b). This sequence of atmospheric responses to remote and local SST changes results in a delay in the arrival of the precipitation maximum over SCS relative to model climatology (Fig. 6a), and prolonged Meiyu-Baiu activity at WNP near 30°N (Fig. 11a).

Over SCS and WNP, the ascent forced remotely by SST changes in the equatorial Pacific during May(1) of cold events (Fig. 9d) more than compensates the subsidence due to local SST forcing (Fig. 9e), thus leading to low-level cyclonic and positive precipitation anomalies over SCS and WNP in this

period (Fig. 8f). The cold anomaly in the equatorial Pacific persists and penetrates farther westward during May(1)-Jul(1) (Fig. 7b), so that SST forcings in the equatorial Pacific and SCS/WNP domains cooperate with each other in generating subsidence and below-normal rainfall over SCS in Jul(1) (Figs. 10d,e). These changes during cold events account for the occurrence of the precipitation peak over SCS in early summer, and the dry conditions in this region thereafter (Fig. 6a). Weakening of the climatological anticyclone over the subtropical WNP (Figs. 8f,h) also leads to decreased intensity of the Meiyu-Baiu rainband in the 120°-150°E sector during cold events (Fig. 11c).

We have devoted our attention to the impacts of ENSO on the variability of the SCS/WNP monsoon in the summer of Year(1), i.e., several months *after* the typical El Niño and La Niña events have reached their peak strengths. Diagrams analogous to Figs. 6 and 11 have been plotted using model data for Year(0). The latter results (not shown) indicate that most of the precipitation anomalies in the SCS/WNP region are less distinctive or organized than their counterparts in Year(1). The summer of Year(0) corresponds to the developing stage of typical ENSO events in CM2.1. The SST anomalies in the SCS/WNP sector are not yet established by the atmospheric bridge mechanism. The feeble atmospheric signals in SCS/WNP during the summer of Year(0) may partially be attributed to the weak remote and local SST forcings in this phase of ENSO development.

Both the excessive ENSO intensity, and the spurious shift of the ENSO forcing towards the SCS/WNP region in the CM2.1 simulation, as noted by Wittenberg et al. (2006), may result in too much influence of ENSO on the SCS/WNP monsoon. As noted at the conclusion of Section 5b, the strength of ENSO events may also affect the propagation characteristics of the SST anomalies, which are a key consideration for determining monsoon development over SCS/WNP (see Section 6). In view of the model bias in over-estimating the amplitude of ENSO, the relationships between the SCS/WNP monsoon and ENSO, as delineated from the model analyses in Sections 5 and 6, may be applicable especially to strong ENSO events. Attempts to confirm these relationships by observations are hampered by the limited number of strong ENSO episodes in the data record.

Wu and Wang (2001) have emphasized that the observed northeastward development of the summer monsoon over SCS and WNP does not proceed smoothly with the slow seasonal cycle of SW and SST forcing, but is instead accomplished by a succession of abrupt advances of monsoon rainfall. These authors proposed that the 'multi-stage' character of the observed SCS/WNP monsoon onset primarily results from the superposition of the seasonal cycle and the wet phase of the climatological intraseasonal oscillations (ISO) residing in this region (Wang and Xu 1997). The latter phenomenon has a typical period of about 30 days, and is phase-locked with the calendar, with wet phases occurring in mid-May, mid-June and late July. The timing of these three consecutive wet phases of the ISO in relation to the seasonal march of the background state favorable for convective activity is a key factor for the sudden onsets over SCS, PS and the northeastern portion of WNP, respectively. The present model study is focused on the slow seasonal component of the evolution of the atmospheric and oceanic environment. Determining the extent to which the abrupt nature of the observed monsoon onsets can be mimicked by CM2.1, and understanding the possible role of ISO in the climatological behavior and variability of the SCS/WNP monsoon, requires further diagnosis of the model output.

Acknowledgments. We thank Andrew Wittenberg for several instructive discussions on the dynamical mechanisms affecting ENSO evolution, and for providing detailed comments on a preliminary draft of this manuscript. Supportive and insightful remarks on various drafts have also been kindly offered by Isaac Held and Renguang Wu.

REFERENCES

Adler, R.F., and Coauthors, 2003: The Version 2 Global Precipitation Climatology Project (GPCP) monthly precipitation analysis (1979-present). *J. Hydrometeor.*, **4**, 1147-1167.

Alexander, M.A., N.-C. Lau, and J.D. Scott, 2004: Broadening the atmospheric bridge paradigm: ENSO teleconnections to the tropical West Pacific-Indian Oceans over the seasonal cycle and to the North Pacific in summer. *Earth's Climate: The Ocean-Atmosphere Interaction. AGU Monograph*, **147**, 85-103, American Geophysical Union, C. Wang, S.-P. Xie and J.A. Carton (Eds.).

An, S.-L., and F.-F. Jin, 2004: Nonlinearity and asymmetry of ENSO. *J. Climate*, **17**, 2399-2412.

Beljaars, A.C.M., 1995: The parameterization of surface-fluxes in large-scale models under free convection. *Quart. J. Roy. Meteor. Soc.*, **121**, 255-270.

Chang, C.-P., (Ed.), 2004: *East Asian Monsoon*. *World Scientific Series on Meteorology of East Asia*, **2,** 564 pp**.**

_____, Y. Zhang, and T. Li, 2000a: Interannual and interdecadal variations of the East Asian summer monsoon and tropical Pacific SSTs. Part I: Roles of the subtropical ridge. *J. Climate*, **13**, 4310-4325.

_____, _____, and _____, 2000b: Interannual and interdecadal variations of the East Asian summer monsoon and tropical Pacific SSTs. Part II: Meridional structure of the monsoon. *J. Climate*, **13**, 4326-4340.

Copsey, D., R. Sutton, and J.R. Knight, 2006: Recent trends in sea level pressure in the Indian Ocean region. *Geophys. Res. Lett.*, **33**, L19712, doi:10.1029/2006GL027175.

Delworth, T.L., and Coauthors, 2006: GFDL's CM2 global coupled climate models. Part I: Formulation and simulation characteristics. *J. Climate*, **19**, 643-674.

Ding, Y., 2004: Seasonal march of the East-Asian summer monsoon. *East Asian Monsoon*. *World Scientific Series on Meteorology of East Asia*, **2**, 30-53. World Scientific, C.-P. Chang (Ed.).

_____, and J.C.L. Chan, 2005: The East Asian summer monsoon: an overview. *Meteorol. Atmos. Phys.*, **89**, 117-142.

Douville, H., 2005: Limitations of time-slice experiments for predicting regional climate change over South Asia. *Climate Dyn.*, **24**, 373-391.

GFDL Global Atmospheric Model Development Team, 2004: The new GFDL global atmosphere and land model AM2/LM2: Evaluation with prescribed SST simulations. *J. Climate*, **17**, 4641-4673.

Gill, A.E., 1980: Some simple solutions for heat-induced tropical circulation. *Quart. J. Roy. Meteor. Soc.*, **106**, 447-462.

Griffies, S.M., and M.J. Harrison, R.C. Pacanowski, and A. Rosati, 2003: A technical guide to MOM4. GFDL Ocean Group Tech. Rep. 5, NOAA/Geophysical Fluid Dynamics Laboratory, Princeton NJ, 295 pp.

Guilyardi, E., 2006: El Niño-mean state-seasonal cycle interactions in a multi-model ensemble. *Climate Dyn.*, **26**, 329-348, doi:10.1007/s00382-005-0084-6.

Harrison, D.E., and N.K. Larkin, 1998: El Niño-Southern Oscillation sea surface temperature and wind anomalies, 1946-1993. *Rev. Geophys.*, **36**, 353-400.

Hoerling, M.P., A. Kumar, and M. Zhong, 1997: El Niño, La Niña, and the nonlinearity of their teleconnections. *J. Climate*, **10**, 1769-1786.

Huffman, G.J., R.F. Adler, P. Arkin, A. Chang, R. Ferraro, A. Gruber, J. Janowick, A. McNab, B. Rodolf, and U. Schneider, 1997: The Global Precipitation Climatology Project (GPCP) combined precipitation dataset. *Bull. Amer. Meteor. Soc.*, **78**, 5-20.

Joseph, R., and S. Nigam, 2006: ENSO evolution and teleconnections in IPCC's twentieth-century climate simulations: Realistic representation? *J. Climate*, **19**, 4360-4377.

Klein, S.A., B.J. Soden, and N.-C. Lau, 1999: Remote sea surface temperature variations during ENSO: Evidence for a tropical atmospheric bridge. *J. Climate*, **12**, 917-932.

Larkin, N.K., and D.E. Harrison, 2002: ENSO warm (El Niño) and cold (La Niña) event life cycles: Ocean surface anomaly patterns, their symmetries, asymmetries, and implications. *J. Climate*, **15**, 1118-1140.

Lau, N.-C., and M.J. Nath, 2003: Atmosphere-ocean variations in the Indo-Pacific sector during ENSO episodes. *J. Climate*, **16**, 3-20.

_____, A. Leetmaa, and M.J. Nath, 2008: Interactions between the responses of North American climate to El Niño-La Niña and to the secular warming trend in the Indian-western Pacific Oceans. *J. Climate*, **21**, 476-494.

Lin, S.-J., 2004: A "vertically Lagrangian" finite-volume dynamical core for global models. *Mon. Wea. Rev.*, **132**, 2293-2307.

Milly, P.C.D., and A.B. Shmakin, 2002: Global modeling of land water and energy balances. Part I: The land dynamics (LaD) model. *J. Hydrometeor.*, **3**, 283-299.

Murakami, T., and J. Matsumoto, 1994: Summer monsoon over the Asian continent and western North Pacific. *J. Meteor. Soc. Japan*, **72**, 719-745.

Neelin, J.D., D.S. Battisti, A.C. Hirst, F.-F. Jin, Y. Wakata, T. Yamagata, and S.E. Zebiak, 1998: ENSO theory. J. Geophys. Res., 103, 14262-14290.

Nitta, T., 1987: Convective activities in the tropical western Pacific and their impact on the northern hemisphere summer circulation. *J. Meteor. Soc. Japan*, **65**, 373-390.

Reynolds, R.W., and T.M. Smith, 1994: Improved global sea surface temperature analyses using optimum interpolation. *J. Climate*, **7**, 929-948.

Shen, S., and K.-M. Lau, 1995: Biennial oscillation associated with the East Asian summer monsoon and tropical sea surface temperatures. *J. Meteor. Soc. Japan*, **73**, 105-124.

Uppala, S.M., and Coauthors, 2005: The ERA-40 re-analysis. *Quart. J. Roy. Meteor. Soc.*, **131**, 2961-3012.

Wang, B., 1994: Climatic regimes of tropical convection and rainfall. *J. Climate*, **7**, 1109-1118.

_____, (Ed.), 2006: *The Asian Monsoon*. Springer-Praxis, 787 pp.

_____, and LinHo, 2002: Rainy season of the Asian-Pacific summer monsoon. *J. Climate*, **15**, 386-398.

_____, and X. Xu, 1997: Northern Hemisphere summer monsoon singularities and climatological intraseasonal oscillation. *J. Climate*, **10**, 1071-1085.

Wang, C., and J. Picaut, 2004: Understanding ENSO physics: A review. *Earth's Climate: The Ocean-Atmosphere Interaction. AGU Monograph*, **147**, 21-48, American Geophysical Union, C. Wang, S.-P. Xie and J.A. Carton (Eds.).

Wittenberg, A.T., 2002: ENSO response to altered climates. Ph.D. thesis, Princeton University, 475 pp.

_____, A. Rosati, N.-C. Lau, and J.J. Ploshay, 2006: GFDL's CM2 global coupled climate models. Part III: Tropical Pacific climate and ENSO. *J. Climate*, **19**, 698-722.

Wu, R., 2002: Processes for the northeastward advance of the summer monsoon over the western North Pacific. *J. Meteor. Soc. Japan*, **80**, 67-83.

_____, and B. Wang, 2000: Interannual variability of summer monsoon onset over the western North Pacific and the underlying processes. *J. Climate*, **13**, 2483-2501.

_____, and _____, 2001: Multi-stage onset of the summer monsoon over the western North Pacific. *Climate Dyn.*, **17**, 277-289.

Yu, L., and R.A. Weller, 2007: Objectively analyzed air-sea heat fluxes (OAFLUX) for the global oceans. *Bull. Amer. Meteor. Soc.*, **88**, 527-539.

Zhang, Y.-C., W.B. Rossow, A.A. Lacis, V. Oinas, and M.I. Mishchenko, 2004: Calculation of radiative fluxes from the surface to top of atmosphere based on ISCCP and other global data sets: Refinements of the radiative model and the input data. *J. Geophys. Res.*, **109**, D19105, doi:10.1029/2003JD004457.

Table Caption

Table 1. Spatial correlation coefficients (SCC) between anomalous precipitation pattern in the ENSO+SCS/WNP experiment and the corresponding responses in the ENSO experiment (first row) and SCS/WNP experiment (second row), linear sum of the responses in the ENSO and SCS/WNP experiments (third row), and composites of ENSO events simulated by CM2.1 (fourth row). Results are shown separately for May(1) and Jul(1), and for warm and cold ENSO events. Computations are based on the domain of 20ºS-30ºN, 90ºE-150ºW. Statistical significance of the SCC is assessed using a procedure similar to that outlined in footnote 4 of Lau et al. (2008). Altogether 150 samples are drawn from the 200-year output of the CM2.1 integration, with each sample consisting of 30 months that are randomly chosen. SCC are then computed between all possible (11 175) pairings of these 30-month averages. Threshold values for various percentiles of this population of SCC are noted. SCC values that surpass the thresholds for the 95^{th} and 99^{th} percentiles are indicated using bold italic and underlined bold italic, respectively.

Table 1. Spatial correlation coefficients (SCC) between anomalous precipitation pattern in the ENSO+SCS/WNP experiment and the corresponding responses in the ENSO experiment (first row) and SCS/WNP experiment (second row), linear sum of the responses in the ENSO and SCS/WNP experiments (third row), and composites of ENSO events simulated by CM2.1 (fourth row). Results are shown separately for May(1) and Jul(1), and for warm and cold ENSO events. Computations are based on the domain of 20ºS-30ºN, 90ºE-150ºW. Statistical significance of the SCC is assessed using a procedure similar to that outlined in footnote 4 of Lau et al. (2008). Altogether 150 samples are drawn from the 200-year output of the CM2.1 integration, with each sample consisting of 30 months that are randomly chosen. SCC are then computed between all possible (11 175) pairings of these 30-month averages. Threshold values for various percentiles of this population of SCC are noted. SCC values that surpass the thresholds for the 95th and 99th percentiles are indicated using bold italic and underlined bold italic, respectively.

	May(1)		Jul(1)	
	Warm Event	Cold Event	Warm Event	Cold Event
ENSO	***0.95***	***0.93***	***0.74***	***0.96***
SCS/WNP	-0.01	0.36	***0.53***	***0.62***
Sum of ENSO and SCS/WNP	***0.93***	***0.88***	***0.93***	***0.94***
CM2.1	***0.72***	***0.70***	***0.75***	***0.86***

Figure Captions

Fig. 1. Climatological distributions of precipitation (shading, see scale bar at bottom) and surface wind vector [arrows, see scale above panel (c)], for the two-month periods of (a, c) May-June and (b, d) July-August. Patterns are based on output from CM2.1 (left panels) and observational estimates of the GPCP and ERA40 datasets (right panels). In this figure as well as in Figs. 2-5, the climatological means are computed over the 200-year output from the CM2.1 integration, and over the entire length of record of various observational datasets listed in Section 2.

Fig. 2. Distributions of differences between consecutive 10-day means, as computed by subtracting climatological data for April 21-30 from May 1-10 (first row), May 21-30 from May 31-June 9 (second row), June 20-29 from June 30-July 9 (third row), and July 20-29 from July 30-August 8 (fourth row). Tendency charts are shown for (left column) precipitation (shading) and 850-mb wind vector [arrows, see scale above panel (a)], (middle column) downward shortwave flux, and (right column) upward latent heat flux. Scale bars for precipitation and shortwave/latent heat fluxes are shown in the bottom left and right, respectively. All patterns are based on output from CM2.1. Red line segments in the left panels depict the southwest-to-northeast track of the precipitation signal. In Fig. 4, development along this track is illustrated by taking latitudinal averages over the 10°-zone defined by the red line segments for individual longitudes. The yellow boxes in panel (a) correspond to the boundaries of Sites A and B used for computing the areal averages shown in Fig. 6.

Fig. 3. As in Fig. 2, but for tendencies from June 20-29 to June 30-July 9 based on various observational datasets.

Fig. 4. Variations along the southwest-to-northeast precipitation track in the SCS/PS/WNP region (see red line segments in left panels of Fig. 2) with pentad in the calendar year (ordinate) and

longitude (abscissa). At each longitude, averages are taken over the 10°-latitudinal span of the track, as delimited by the northern and southern red line segments (see Fig. 2) for that longitude. Results are shown for (first row) precipitation (shading) and 850-mb wind vector [arrows, see scale above panel (e)], (second row) downward shortwave flux, (third row) upward latent heat flux, and (fourth row) sea surface temperature. Patterns are based on 5-day averages of climatological data from CM2.1 (left panels) and various observational projects (right panels). In order to accommodate the systematic biases between the model and observations, the range of model values corresponding to given color shade is shifted relative to the range of observational values. Two columns of values (the left for model data, the right for observations) are used to label the scale bars for patterns in the lower three rows. The polarity and magnitude of these offsets reflect the main biases of the simulated values relative to the observations (+10 Wm^{-2} for shortwave flux, +20 Wm^{-2} for latent heat flux, and -0.5°C for sea surface temperature).

Fig. 5. Variations of longitudinal averages over the 120°-150°E zone with latitude (ordinate) and pentad in the calendar year (abscissa). Results are shown for (first row) precipitation (shading) and 850-mb wind vector [arrows, see scale above panel (c)], and (second row) 10-day tendency of downward shortwave flux. Patterns are based on 5-day averages of climatological data from CM2.1 (left panels) and various observational projects (right panels). For a given date, the flux tendencies in the lower panels are computed by subtracting the 2-pentad (10-day) mean prior to this date from the 2-pentad mean after this date.

Fig. 6. Time series of the areal average of precipitation over (a) 8°-18°N 115°-120°E (Site A) and (b) 10°-20°N 125°-130°E (Site B), as computed using pentad data from the CM2.1 simulation for 200-year climatology (black curves), and for Year(1) of selected El Niño (red curves) and La Niña (blue curves) events. Those pentads in which the departures of warm (cold) composites of

precipitation from climatology surpass the 95% significance level are indicated by red (blue) circles. The boundaries of Sites A and B are shown in Fig. 2a.

Fig. 7. Variations of latitudinal averages of sea surface temperature anomaly over the 5°S-5°N zone with time (ordinate) and longitude (abscissa), for composites over (a) warm and (b) cold ENSO events. Patterns are based on monthly means from the CM2.1 simulation. Positive (negative) anomaly values at the 95% significance level are indicated by solid (dashed) purple contours.

Fig. 8. Distributions of the anomalies of (first and third rows) 200-mb velocity potential (contours; interval: 0.5×10^6 m^2s^{-1}; solid and dashed contours indicate positive and negative values, respectively) and divergent wind vector [arrows, see scale above panels (e) and (g)], and sea surface temperature (shading), and (second and fourth rows) 850-mb flow field (streamlines) and precipitation (shading). Patterns are based on monthly means from the CM2.1 simulation, for composites over the warm (left panels, with red frames) and cold (right panels, with blue frames) ENSO events. Results are presented for the periods of May(1) (upper half, with yellow background) and Jul(1) (lower half, with green background). Only those sea surface temperature and precipitation anomalies that exceed the 95% significance level are depicted with color shading; those locations where the anomalies do not meet this criterion are left blank. Velocity potential anomalies above (below) the 95% significance level are indicated using black (gray) contours. The scale bar used for the color shading in each row is shown at the right edge of that row.

Fig. 9. Distributions of the anomalies of 200-mb velocity potential (contours; interval: 0.5×10^6 m^2s^{-1}; solid and dashed contours indicate positive and negative values, respectively) and divergent wind vector (arrows), and precipitation (shading). Patterns are based on responses of AM2.1 to composite warm (left panels, with red frames) and cold (right panels, with blue frames) sea

surface temperature forcings in May(1). Responses to forcings in the ENSO, SCS/WNP and ENSO+SCS/WNP experiments are displayed in the first, second and third row, respectively. Only those precipitation anomalies that exceed the 90% significance level are depicted with color shading; those locations where the anomalies do not meet this criterion are left blank. Velocity potential anomalies above (below) the 95% significance level are indicated using black (gray) contours. The scale bar used for the color shading in all panels is shown at the bottom. The scale for plotting the wind vectors in all panels is shown at the upper right of panel (d). The red borders in panels (d) and (f) indicate the western portion of the domain for prescription of anomalous SST forcing in the ENSO and ENSO+SCS/WNP experiment, respectively (the eastern portion of this forcing domain, not shown, extends all the way to the American coasts). The red borders in panel (e) indicate the domain for anomalous SST forcing in the SCS/WNP experiment.

Fig. 10. As in Fig. 9, but for responses to sea surface temperature forcings in Jul(1).

Fig. 11. Variations of longitudinal averages of precipitation anomalies over the 120°-150°E zone with latitude (ordinate) and time in Year(1) (abscissa). Patterns are based on 5-day means from the CM2.1 simulation (top row) and the response of AM2.1 to sea surface temperature forcing in the ENSO+SCS/WNP experiment (bottom row). Results are presented for signals in composite warm (left panels, with red frames) and cold (right panels, with blue frames) ENSO events. Positive (negative) anomaly values at the 95% significance level are indicated by solid (dashed) purple contours. The scale bar used for the color shading is shown at the bottom.

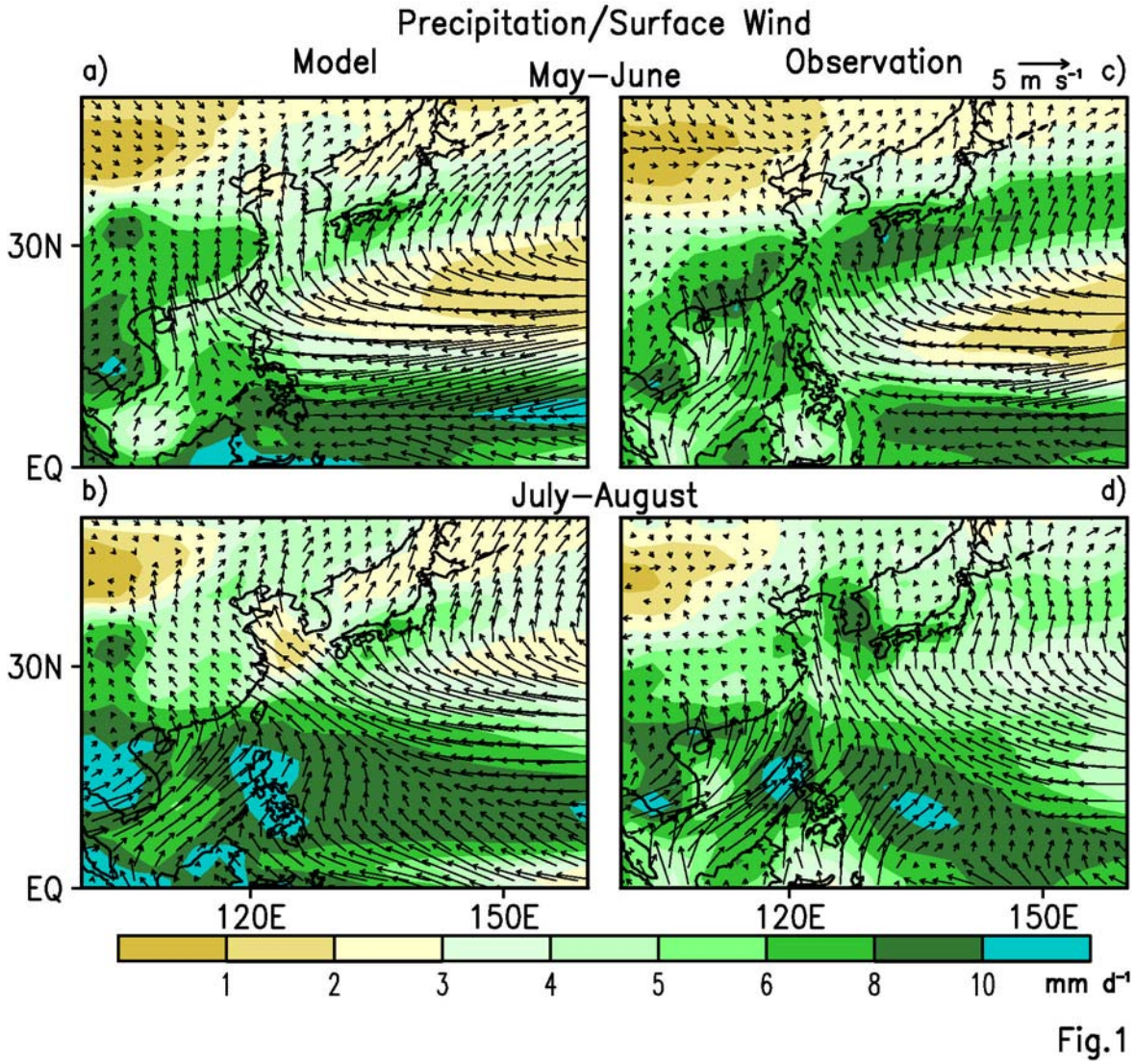

Fig. 1. Climatological distributions of precipitation (shading, see scale bar at bottom) and surface wind vector [arrows, see scale above panel (c)], for the two-month periods of (a, c) May-June and (b, d) July-August. Patterns are based on output from CM2.1 (left panels) and observational estimates of the GPCP and ERA40 datasets (right panels). In this figure as well as in Figs. 2-5, the climatological means are computed over the 200-year output from the CM2.1 integration, and over the entire length of record of various observational datasets listed in Section 2.

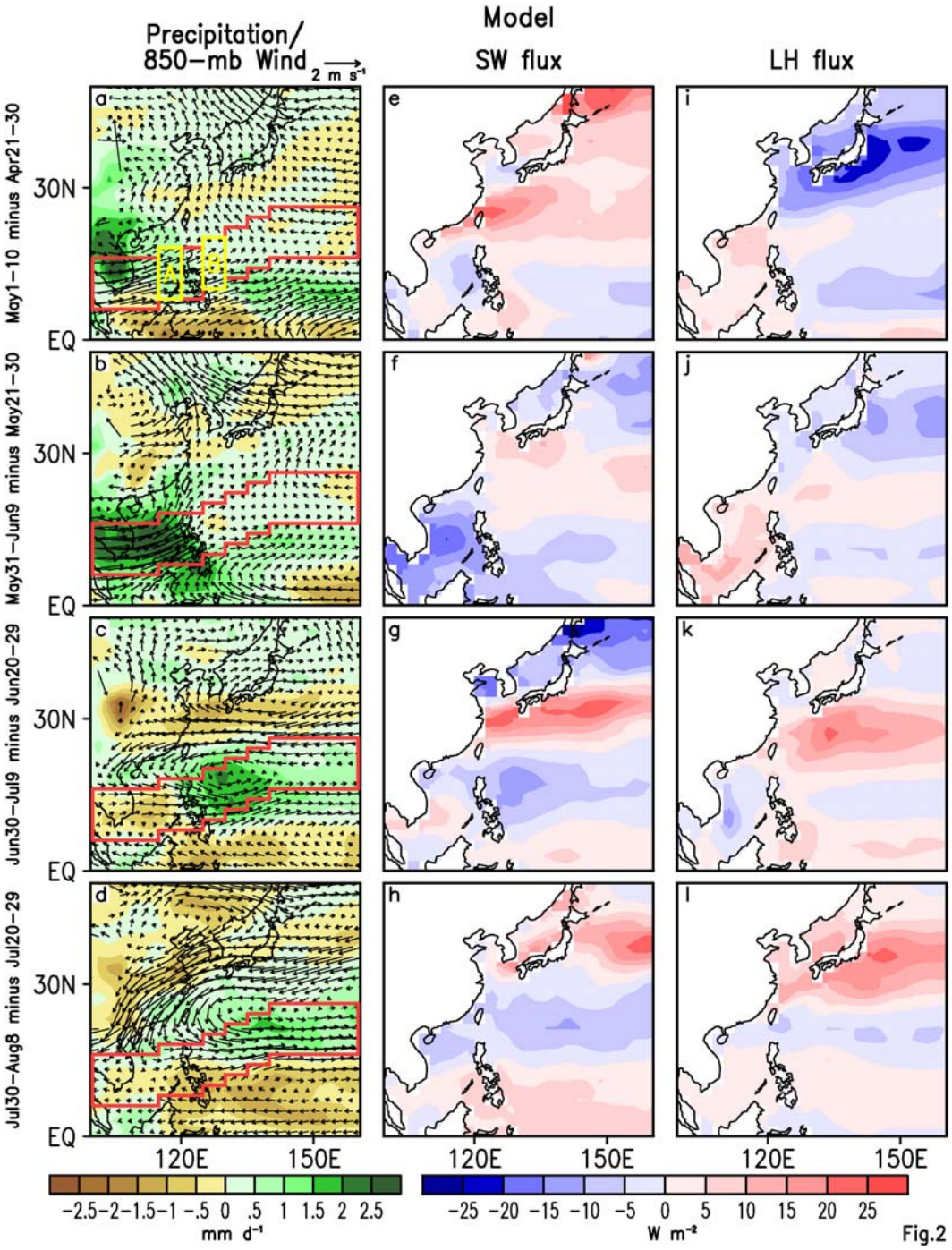

Fig. 2. Distributions of differences between consecutive 10-day means, as computed by subtracting climatological data for April 21-30 from May 1-10 (first row), May 21-30 from May 31-June 9 (second row), June 20-29 from June 30-July 9 (third row), and July 20-29 from July 30-August 8 (fourth row). Tendency charts are shown for (left column) precipitation (shading) and 850-mb wind vector [arrows, see scale above panel (a)], (middle column) downward shortwave flux, and (right column) upward latent heat flux. Scale bars for precipitation and shortwave/latent heat fluxes are shown in the bottom left and right, respectively. All patterns are based on output from CM2.1. Red line segments in the left panels depict the southwest-to-northeast track of the precipitation signal. In Fig. 4, development along this track is illustrated by taking latitudinal averages over the 10°-zone defined by the red line segments for individual longitudes. The yellow boxes in panel (a) correspond to the boundaries of Sites A and B used for computing the areal averages shown in Fig. 6.

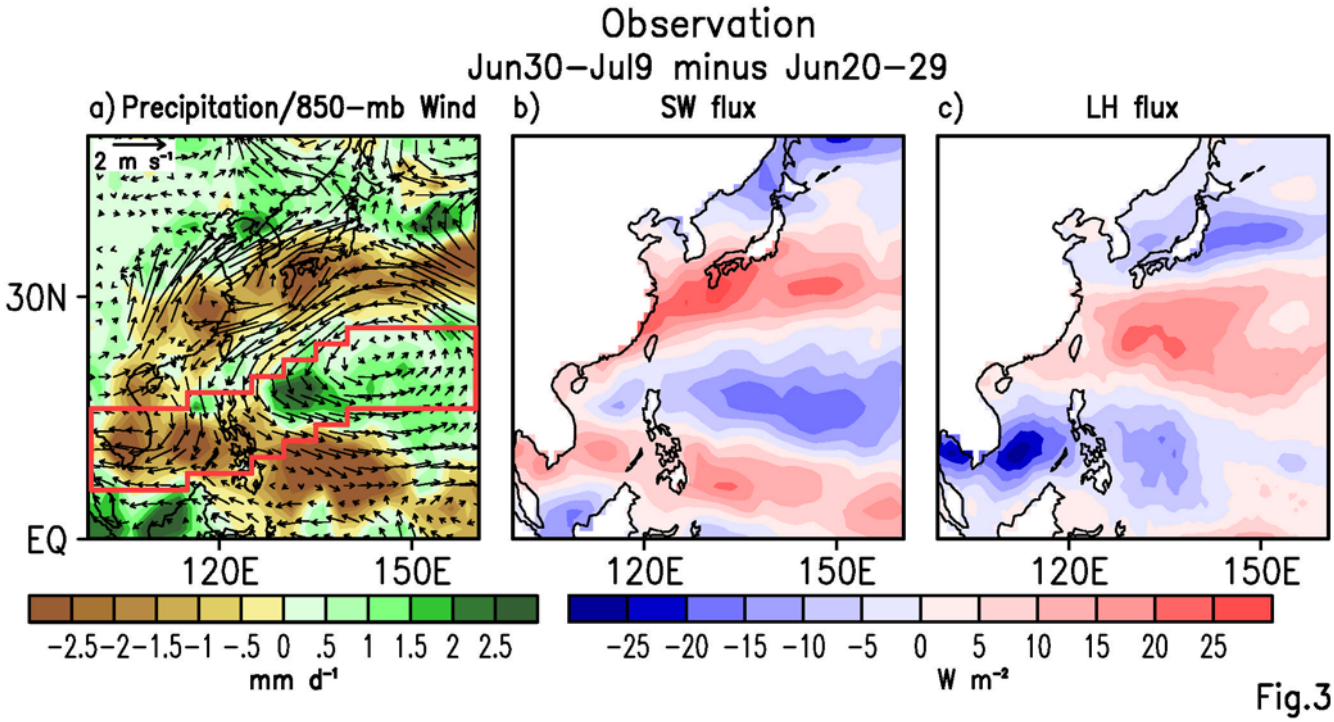

Fig. 3. As in Fig. 2, but for tendencies from June 20-29 to June 30-July 9 based on various observational datasets.

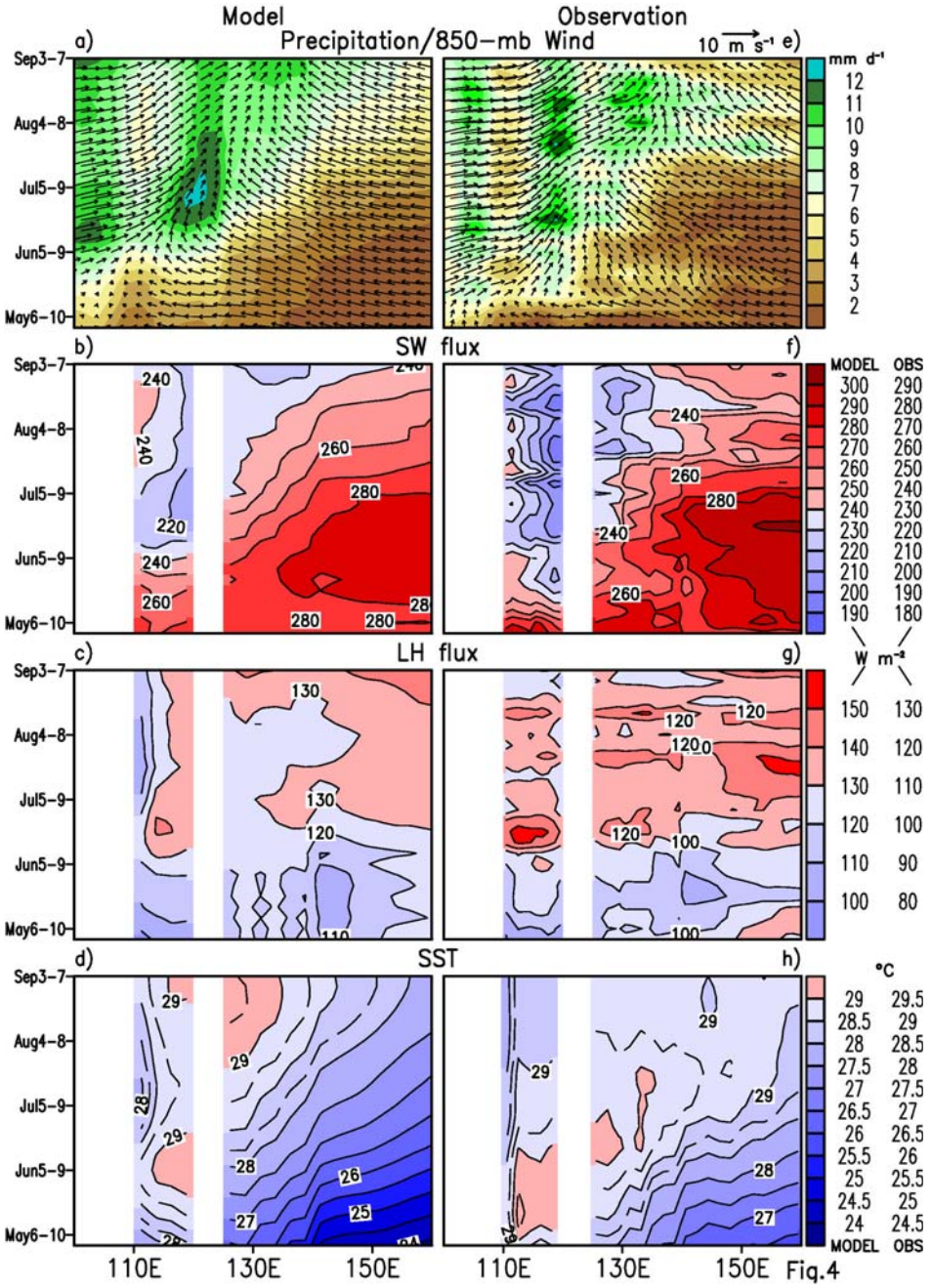

Fig. 4. Variations along the southwest-to-northeast precipitation track in the SCS/PS/WNP region (see red line segments in left panels of Fig. 2) with pentad in the calendar year (ordinate) and longitude (abscissa). At each longitude, averages are taken over the 10°-latitudinal span of the track, as delimited by the northern and southern red line segments (see Fig. 2) for that longitude. Results are shown for (first row) precipitation (shading) and 850-mb wind vector [arrows, see scale above panel (e)], (second row) downward shortwave flux, (third row) upward latent heat flux, and (fourth row) sea surface temperature. Patterns are based on 5-day averages of climatological data from CM2.1 (left panels) and various observational projects (right panels). In order to accommodate the systematic biases between the model and observations, the range of model values corresponding to given color shade is shifted relative to the range of observational values. Two columns of values (the left for model data, the right for observations) are used to label the scale bars for patterns in the lower three rows. The polarity and magnitude of these offsets reflect the main biases of the simulated values relative to the observations (+10 Wm^{-2} for shortwave flux, +20 Wm^{-2} for latent heat flux, and -0.5°C for sea surface temperature).

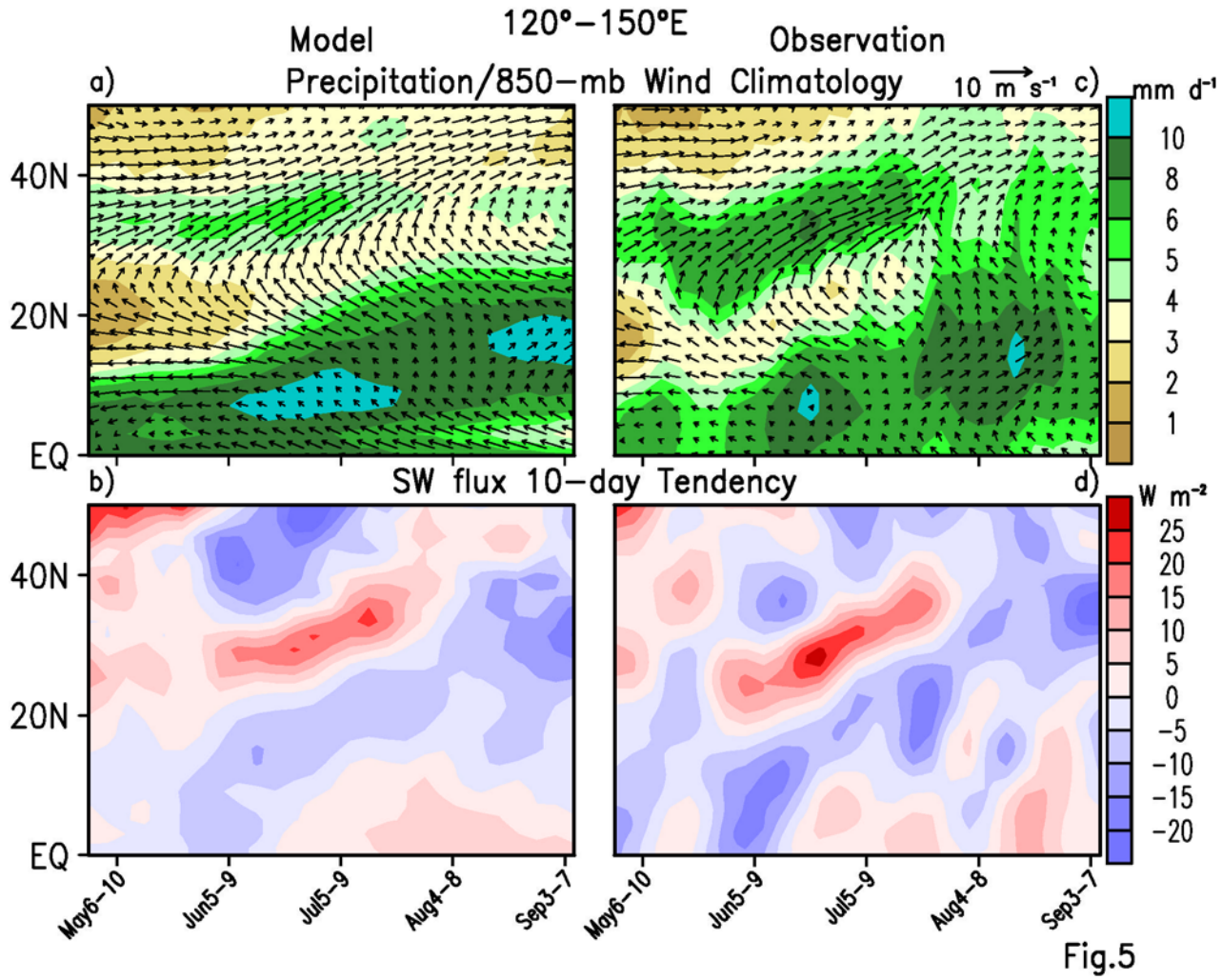

Fig. 5. Variations of longitudinal averages over the 120°-150°E zone with latitude (ordinate) and pentad in the calendar year (abscissa). Results are shown for (first row) precipitation (shading) and 850-mb wind vector [arrows, see scale above panel (c)], and (second row) 10-day tendency of downward shortwave flux. Patterns are based on 5-day averages of climatological data from CM2.1 (left panels) and various observational projects (right panels). For a given date, the flux tendencies in the lower panels are computed by subtracting the 2-pentad (10-day) mean prior to this date from the 2-pentad mean after this date.

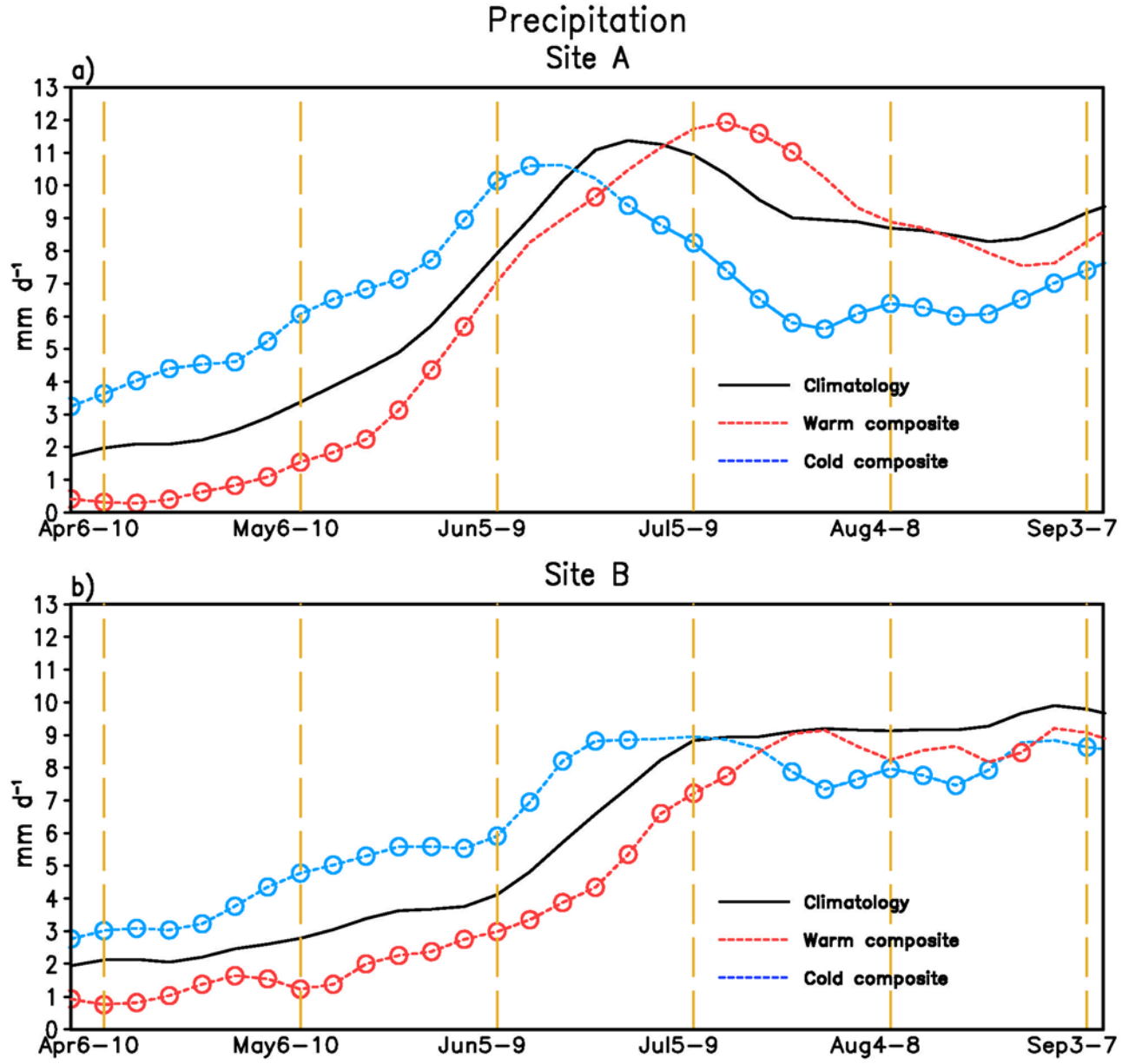

Fig.6

Fig. 6. Time series of the areal average of precipitation over (a) 8°-18°N 115°-120°E (Site A) and (b) 10°-20°N 125°-130°E (Site B), as computed using pentad data from the CM2.1 simulation for 200-year climatology (black curves), and for Year(1) of selected El Niño (red curves) and La Niña (blue curves) events. Those pentads in which the departures of warm (cold) composites of precipitation from climatology surpass the 95% significance level are indicated by red (blue) circles. The boundaries of Sites A and B are shown in Fig. 2a.

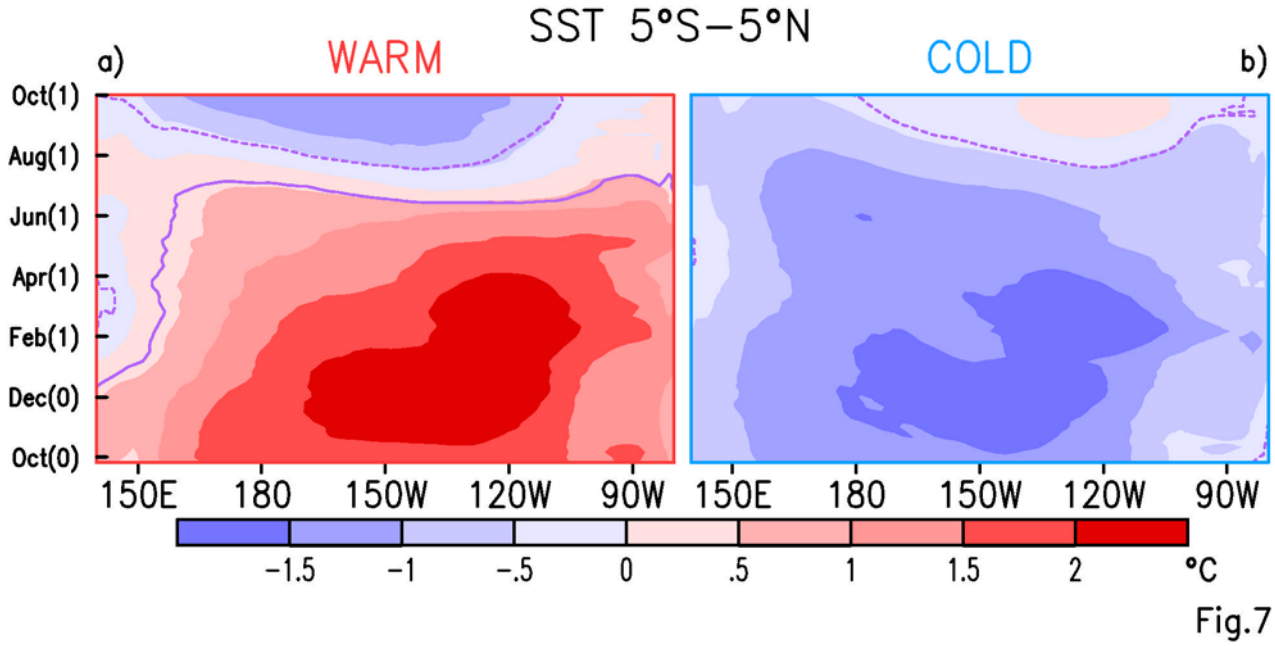

Fig. 7. Variations of latitudinal averages of sea surface temperature anomaly over the 5°S-5°N zone with time (ordinate) and longitude (abscissa), for composites over (a) warm and (b) cold ENSO events. Patterns are based on monthly means from the CM2.1 simulation. Positive (negative) anomaly values at the 95% significance level are indicated by solid (dashed) purple contours.

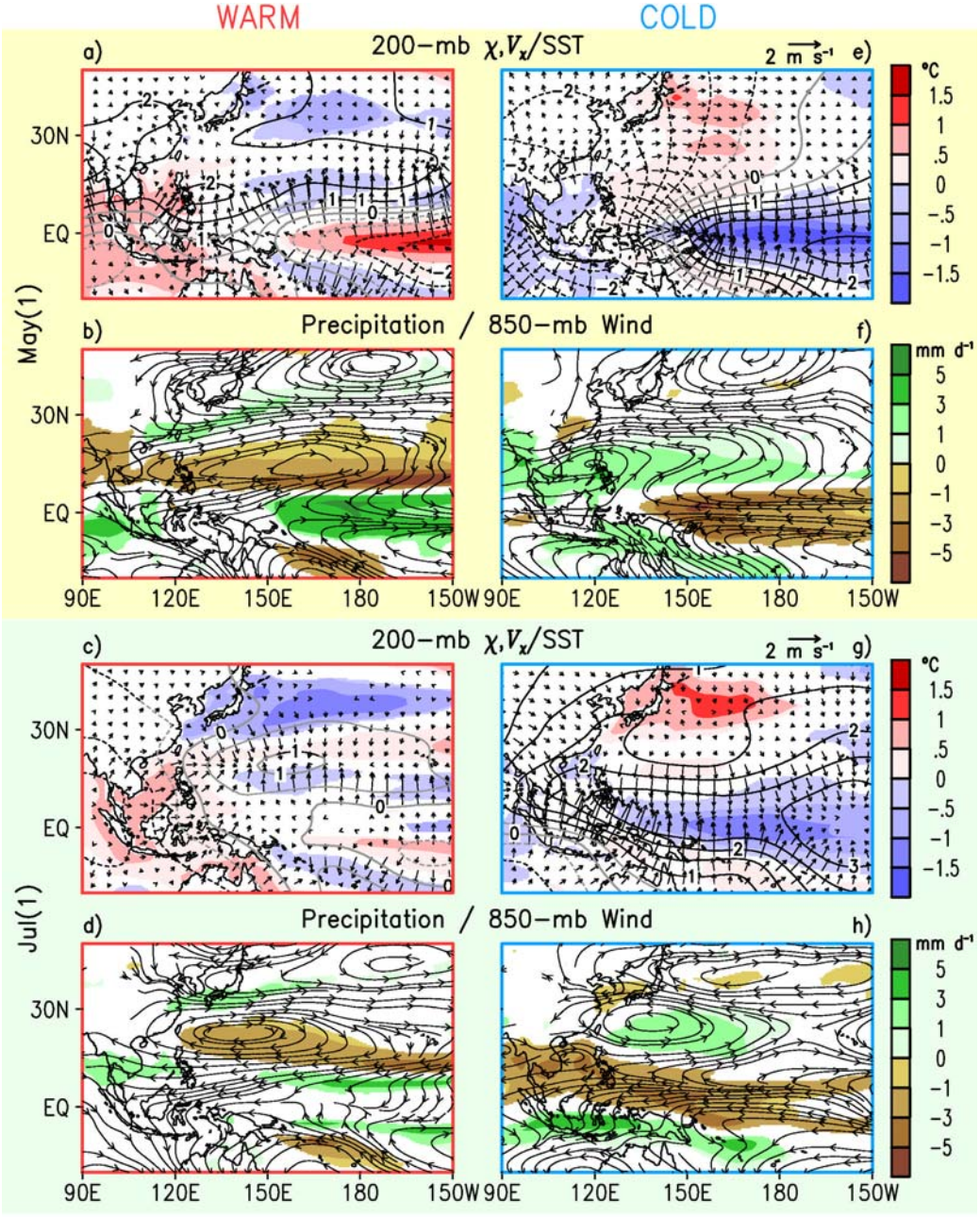

Fig.8

Fig. 8. Distributions of the anomalies of (first and third rows) 200-mb velocity potential (contours; interval: 0.5×10^6 m^2s^{-1}; solid and dashed contours indicate positive and negative values, respectively) and divergent wind vector [arrows, see scale above panels (e) and (g)], and sea surface temperature (shading), and (second and fourth rows) 850-mb flow field (streamlines) and precipitation (shading). Patterns are based on monthly means from the CM2.1 simulation, for composites over the warm (left panels, with red frames) and cold (right panels, with blue frames) ENSO events. Results are presented for the periods of May(1) (upper half, with yellow background) and Jul(1) (lower half, with green background). Only those sea surface temperature and precipitation anomalies that exceed the 95% significance level are depicted with color shading; those locations where the anomalies do not meet this criterion are left blank. Velocity potential anomalies above (below) the 95% significance level are indicated using black (gray) contours. The scale bar used for the color shading in each row is shown at the right edge of that row.

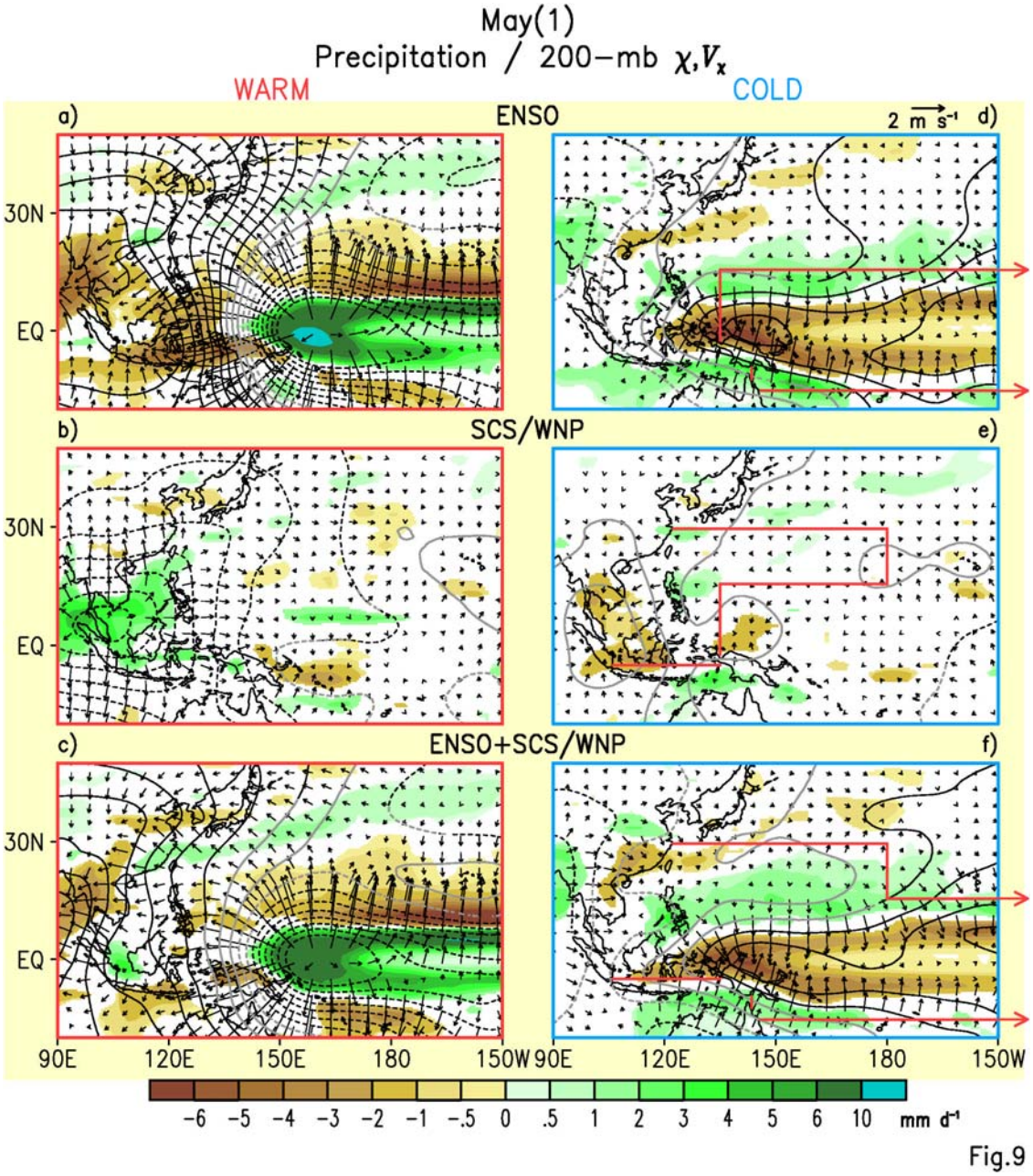

Fig.9

Fig. 9. Distributions of the anomalies of 200-mb velocity potential (contours; interval: 0.5×10^6 m^2s^{-1}; solid and dashed contours indicate positive and negative values, respectively) and divergent wind vector (arrows), and precipitation (shading). Patterns are based on responses of AM2.1 to composite warm (left panels, with red frames) and cold (right panels, with blue frames) sea surface temperature forcings in May(1). Responses to forcings in the ENSO, SCS/WNP and ENSO+SCS/WNP experiments are displayed in the first, second and third row, respectively. Only those precipitation anomalies that exceed the 90% significance level are depicted with color shading; those locations where the anomalies do not meet this criterion are left blank. Velocity potential anomalies above (below) the 95% significance level are indicated using black (gray) contours. The scale bar used for the color shading in all panels is shown at the bottom. The scale for plotting the wind vectors in all panels is shown at the upper right of panel (d). The red borders in panels (d) and (f) indicate the western portion of the domain for prescription of anomalous SST forcing in the ENSO and ENSO+SCS/WNP experiment, respectively (the eastern portion of this forcing domain, not shown, extends all the way to the American coasts). The red borders in panel (e) indicate the domain for anomalous SST forcing in the SCS/WNP experiment.

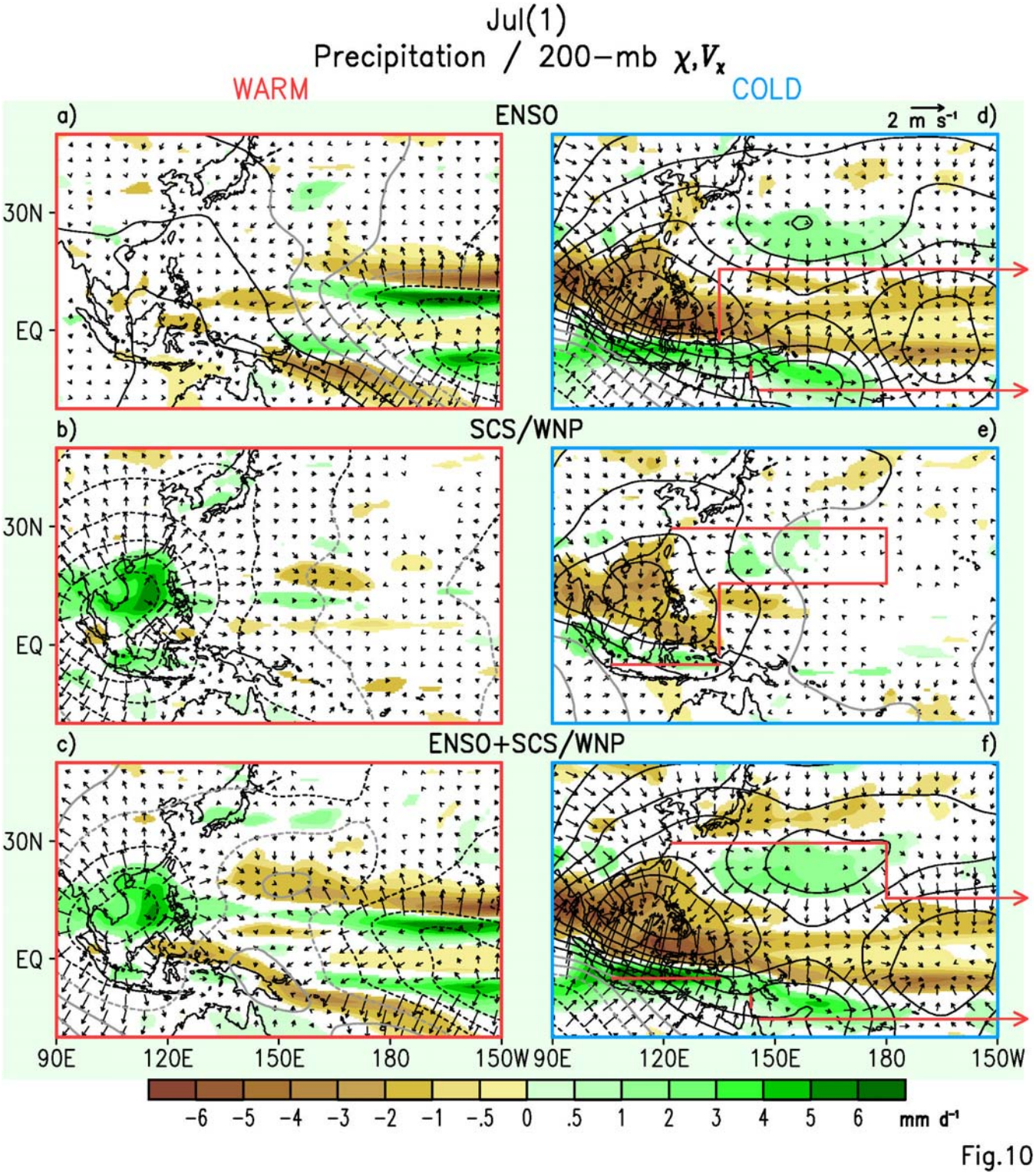

Fig. 10. As in Fig. 9, but for responses to sea surface temperature forcings in Jul(1).

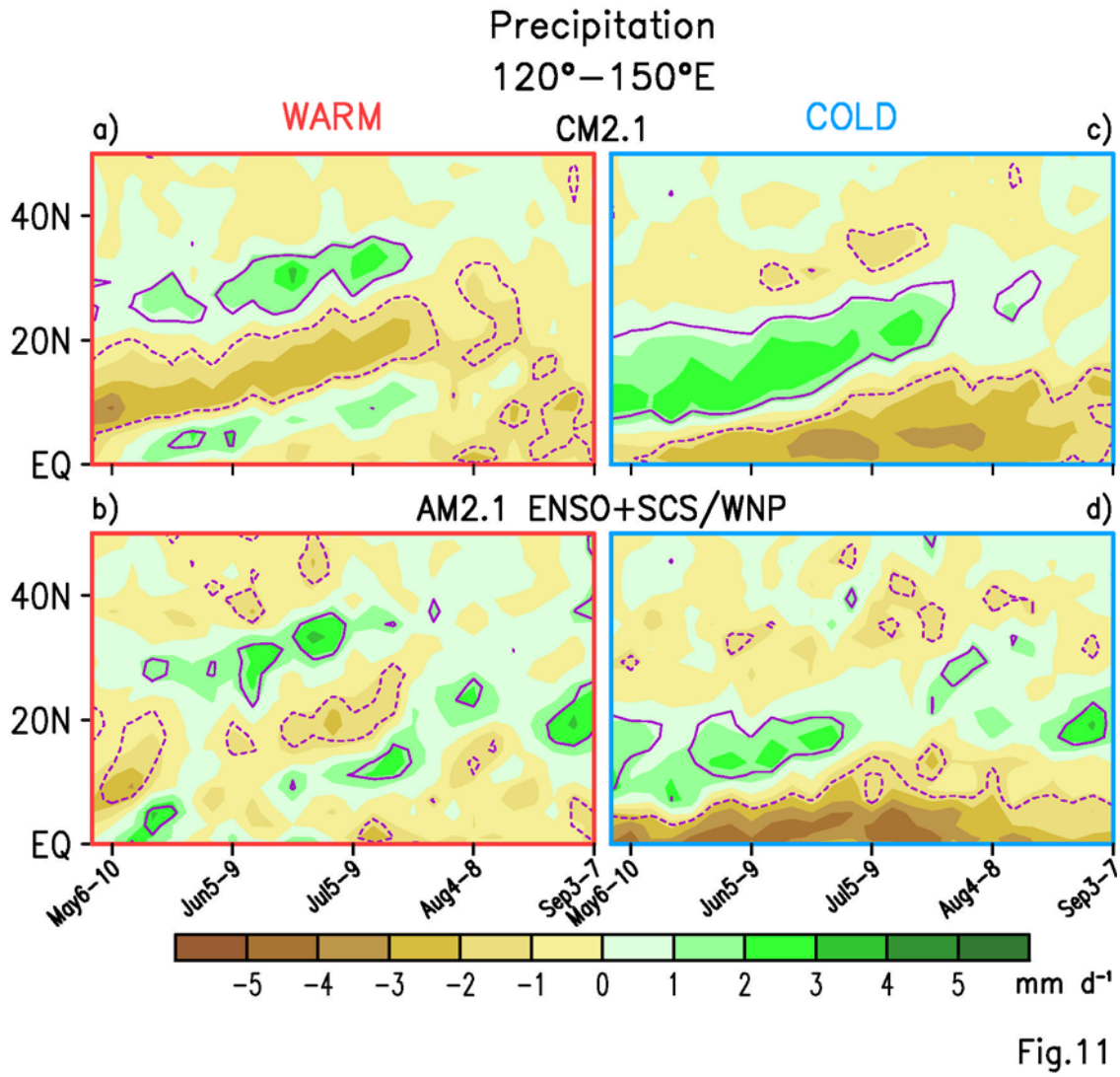

Fig.11

Fig. 11. Variations of longitudinal averages of precipitation anomalies over the 120°-150°E zone with latitude (ordinate) and time in Year(1) (abscissa). Patterns are based on 5-day means from the CM2.1 simulation (top row) and the response of AM2.1 to sea surface temperature forcing in the ENSO+SCS/WNP experiment (bottom row). Results are presented for signals in composite warm (left panels, with red frames) and cold (right panels, with blue frames) ENSO events. Positive (negative) anomaly values at the 95% significance level are indicated by solid (dashed) purple contours. The scale bar used for the color shading is shown at the bottom.